ACS OMEGA

http://pubs.acs.org/journal/acsodf

Article

# A Novel Approach to Prepare Cellulose-*g*-Hydroxyapatite Originated from Natural Sources as an Efficient Adsorbent for Heavy Metals: Batch Adsorption Optimization via Response Surface Methodology

Salah Eddine Marrane, Karim Dänoun,* Dalia Allouss, Said Sair, Badr-Eddine Channab, Abdallah Rhihil, and Mohamed Zahouily*

Cite This: *ACS Omega* 2022, 7, 28076−28092

Read Online

ACCESS | Metrics & More | Article Recommendations | Supporting Information

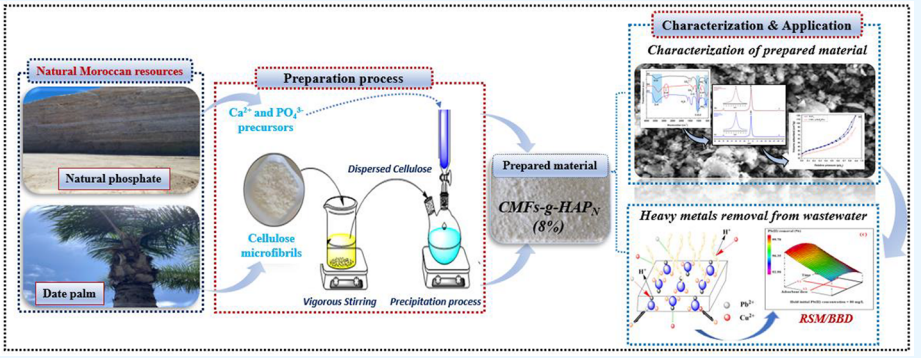


**ABSTRACT:** In the present research, we describe a novel approach for in situ synthesis of cellulose microfibrils-*grafted*-hydroxyapatite (CMFs-*g*-$HAP_N$ (8%)) as an adsorbent using phosphate rock and date palm petiole wood as alternative and natural Moroccan resources. The synthesized CMFs-*g*-$HAP_N$ (8%) was extensively characterized by several instrumental techniques like thermogravimetry analysis, Fourier transform infrared spectroscopy, X-ray diffraction, $^{31}P$ nuclear magnetic resonance, scanning electron microscopy, and Brunauer−Emmett−Teller analysis. The developed adsorbent was used to remove Pb(II) and Cu(II) from aqueous solutions. The influences of different adsorption parameters such as contact time, initial metal concentration, and amount of adsorbent were also investigated thoroughly using response surface methodology in order to optimize the batch adsorption process. The results confirmed that the adsorption process follows a polynomial quadratic model as high regression parameters were obtained ($R^2$ value = 99.8% for Pb(II) and $R^2$ value = 92.6% for Cu(II)). According to kinetics and isotherm modeling, the adsorption process of both studied ions onto CMFs-*g*-$HAP_N$ (8%) followed the pseudo-second-order model, and the equilibrium data at 25 °C were better fitted by the Langmuir model. The maximum adsorption capacities of the CMFs-*g*-$HAP_N$ (8%) adsorbent toward Pb(II) and Cu(II) are 143.80 and 83.05 mg/g, respectively. Moreover, the experiments of multicycle adsorption/desorption indicated that the CMFs-*g*-$HAP_N$ (8%) adsorbent could be regenerated and reused up to three cycles. The high adsorption capacities of both studied metals and regeneration performances of the CMFs-*g*-$HAP_N$ (8%) suggest its applicability as a competitive adsorbent for large-scale utilization.

## 1. INTRODUCTION

Owing to industrialization processes and fast-moving economic development in recent decades, the environmental contamination caused by heavy metals has become one of the serious concerns over the world.[1] The origin of this environmental problem derives principally from various industrial activities,[1] which produce enormous quantities of wastewater containing diverse concentrations of heavy metals into the environment.[2,3] These heavy metals are carcinogenic agents and pose a grave hazard to the living population in view of their persistent, nondegradable, and accumulative nature.[4−6] For instance, lead and copper are among the most common pollutants present in industrial effluents which cause considerable effects on the human body even at a low concentration.[7−9] According to the U.S. Environmental Action Group, industrial effluents have

Received: April 5, 2022
Accepted: June 28, 2022
Published: August 5, 2022

menaced the health of more than 10 million people in many countries.[10] For these reasons, much attention has recently been devoted to wastewater treatment, and many environmental policies insist that the effluents containing hazardous heavy metals must be treated to certain concentrations before their discharges into receiving bodies. Several techniques have been utilized to remove these hazardous pollutants from aqueous solutions over the years including chemical precipitation,[11] ion exchange,[12] electrochemical treatment,[13] membrane filtration technology,[14] and solvent extraction.[15] Nevertheless, all these techniques have inherent disadvantages and limitations in their application such as high reagent and energy requirements, incomplete metal removal, and generation of toxic sludge or other waste products,[16−18] whereas the application of the adsorption process for water treatment has received considerable attention during the last few years due to its several important advantages, including low cost, high efficiency, easy handling, availability of different adsorbents, and large-scale feasibility with avoidance of the formation of secondary pollutants compared to other conventional techniques.[19,20] Furthermore, this process has been demonstrated to be widely efficient for removing a series of contaminants such as heavy metals, dyes, phenol-derived compounds, and other emerging contaminants that can be encountered in surface water, groundwater, and industrial wastewaters even in low concentration ranges from ng $L^{-1}$ to mg $L^{-1}$.[21−23] From a process engineering point of view, the development and choice of the adsorbent material are key points to design an adsorption process for water treatment.[24−26]According to the U.S. Environmental Protection Agency, activated carbon is one of the most popular commercial adsorbents for the removal of a variety of toxic substances from industrial wastewater regarding their porous structures and large surface areas.[21] Unfortunately, the high cost of their manufacture limits their use in large-scale levels. Accordingly, considerable effort has been devoted during the last few years to develop green materials for water remediation with low cost, low energy input, and no hazardous byproducts. Among them, hydroxyapatite (HAP) is becoming a promising and potential candidate adsorbent owing to its specific structure, ionic exchange property, and adsorption affinity to various heavy metal ions including Pb(II), Zn(II), Cu(II), Cd(II), and Co(II).[22,24] Synthetic hydroxyapatite can be obtained via different techniques such as wet methods (hydrolysis, hydrothermal, emulsion, sonochemical, and chemical precipitation), dry methods (solid-state and mechanochemical), and high-temperature processes (pyrolysis and combustion). Nevertheless, some of these synthetic routes suffer from several drawbacks because they involve long and complex steps to produce the desired product. Moreover, many chemical reagents seem to be necessary making the process more costly.[27] To overcome these limitations, several studies have been reported in the preparation of natural hydroxyapatite from byproducts[28] and biological[29] and mineral sources.[30] In this respect, Moroccan natural phosphate was selected in this work as a raw material for hydroxyapatite preparation because of its low cost and its natural abundance. In fact, Morocco is the largest phosphate producer in the world; it contains about 75% of the world's estimated reserves, which needs to be valorized.[31] They can be employed not only as fertilizers but also as catalysts in a wide range of organic transformation.[32,33] In addition to the phosphate resource, Morocco has sizable reserves of the date palm; this resource plays a vital role in the economic and social lives of the oasis inhabitants. Nevertheless, the exploitation of this natural resource also generates a significant quantity of wastes that needs to be properly valorized in order to reduce the environmental pollution impacts. Therefore, different parts of date palm waste can thus be used to develop new sustainable bioproducts such as cellulose. Nowadays, cellulose and its derivatives have been widely used as efficient adsorbents in environmental pollutant removal including heavy metals and organic pollutants.[2,4,34] The broad utilization of cellulose as an adsorbent is principally due to its low cost, eco-friendliness, sustainability, biodegradability, and ability to be modified.[35] More recently, merging two natural materials has become an increasingly interesting approach for the development of new biomaterials, which often exhibit combinations of properties that could not be achieved by an individual material. In this light, Fernando et al. investigated the sorption proprieties of neat HAP nanoparticles in the removal of lead from aqueous solutions[36] and showed that the adsorption capacity is close to 83 mg $g^{-1}$, while Chen et al. examined the lead removal efficiency of cellulose (BC) fibers, which was found to be 22.56 mg $g^{-1}$.[37] In another work, Núñez et al. proved that the combination of these two natural materials in a HAP-BC composite could increase the Pb(II) uptake to 192.3 mg $g^{-1}$.[38]

On the other hand, the adsorption process implies the interaction of many operational variables in a nonlinear way. In such a case, the conventional method of adsorption optimization is inefficient as it demands many experimental runs and therefore is time-consuming. Furthermore, this method fails to describe the interactive effects of all operational parameters involved in the adsorption process. To bridge these restrictions, several researchers have used statistical experimental designs comprising response surface methodology (RSM) to evaluate the influence of different parameters on the adsorption process. RSM is considered as a potential statistical tool for developing models and investigating the influence of multiple variable processes simultaneously. Among the various matrix designs, Box−Behnken design (BBD) has been widely applied in the optimization of chemical and physical processes thanks to its design and excellent outcomes.[39]

Based on these considerations and in continuation of our ongoing program to develop an interesting low-cost material,[40−47]we describe in this paper, our novel approach to synthesize a cellulose microfibrils-*grafted*-hydroxyapatite (CMFs-*g*-$HAP_N$ (8%)) as an adsorbent via an in situ wet chemical process using phosphate rock and date palm petiole as alternative and natural Moroccan resources and evaluate its performance in the removal of Pb(II) and Cu(II) via batch adsorption from aqueous solutions. Subsequently, the adsorption process was optimized by varying three process variables, namely, adsorbent dosage, contact time, and initial metal concentration using BBD. The effect of coexisting cations ($Na^+$, $Mg^{2+}$, and $Ca^{2+}$ ions) on the removal efficiencies of Pb(II) and Cu(II) ions onto CMFs-*g*-$HAP_N$ (8%) was also investigated in order to assess its selectivity and maintainability in simulated wastewater. Kinetics, isotherms, and thermodynamic studies of the adsorption process were also investigated in order to understand the adsorption mechanisms. Desorption and the reuse of our prepared material were also studied.

## 2. RESULTS AND DISCUSSION

**2.1. Characterization of Prepared Materials.** The crystallinity and phase purity of the obtained $CMF_S$, $HAP_N$,



https://doi.org/10.1021/acsomega.2c02108
ACS Omega 2022, 7, 28076−28092

and CMFs-*g*-$HAP_N$ (8%) samples were examined using the X-ray diffraction (XRD) technique. From Figure 1a, the

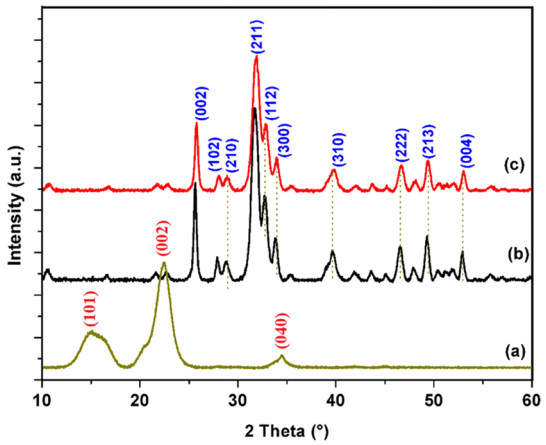


**Figure 1.** XRD patterns of (a) CMFs, (b) $HAP_N$, and (c) CMFs-*g*-$HAP_N$ (8%).

diffraction pattern of CMFs presents two intense peaks at $2\theta$ = 14.8°(101) and 22.7°(002) attributed to the partly crystalline nature of cellulose I.[48] After the grafting process, these crystalline peaks disappeared in the prepared CMFs-*g*-$HAP_N$ (8%) (Figure 1c), which can be due to the electrostatic interactions among the anionic functional groups of CMFs and positive calcium in solution precursor ions.[49] Moreover, the XRD pattern of CMFs-*g*-$HAP_N$ (8%) showed clearly that all other peaks related to the characteristic peaks of $HAP_N$ (Figure 1b) according to PDF card N°00-064-0738 are presented, indicating the formation of the CMFs-*g*-$HAP_N$ (8%) hybrid material. Furthermore, the average size of the crystallites calculated from the Scherrer model of the prepared samples $HAP_N$ and CMFs-*g*-$HAP_N$ (8%) is respectively about 19.8 and 16 nm; these results indicate a significant decrease in the crystallite size due to the grafting process of the CMFs on the surface of $HAP_N$.

The FTIR spectra of the $HAP_N$, extracted cellulose, and CMFs-*g*-$HAP_N$ (8%) are presented in Figure 2. As shown in Figure 2a, the main characteristic peaks of $HAP_N$ that appeared at 547, 601, and 1032 $cm^{-1}$ were assigned to $PO_4^{3-}$, while the sharp peak that appeared at 3571 $cm^{-1}$ was due to the

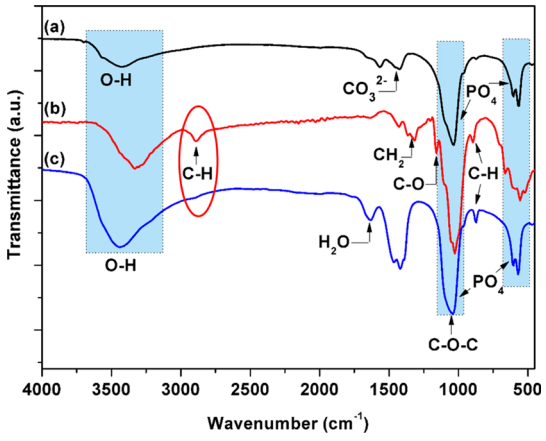


**Figure 2.** Fourier transform infrared (FTIR) spectra of $HAP_N$ (a), extracted cellulose (b), and CMFs-g-$HAP_N$ (8%) (c).

structural OH groups of the apatite.[50] Additionally, weak bands appearing in the range of 1473−1419 $cm^{-1}$ can be attributed to the nonsymmetric stretching vibrations of carbonate ions formed during the preparation of $HAP_N$. After surface grafting (Figure 2c), the obtained CMFs-*g*-$HAP_N$ (8%) has a similar peak to that of the starting materials with shifting toward high frequencies. The O−H band shifts to a higher wavelength than that of cellulose and the O−P−O showed a broader band that extends from 547 to 601, also we can observe the P−O stretching band in the CMFs-*g*-$HAP_N$ (8%) appearing at 1056 $cm^{-1}$ while in $HAP_N$ it showed up at 1032 $cm^{-1}$. The increase in the frequency of these bands indicates the presence of interactions between the surface of $HAP_N$ and CMF groups.

Furthermore, solid-state $^{31}P$ nuclear magnetic resonance (NMR) spectroscopy was performed in view to gain additional information about the purity of CMFs-*g*-$HAP_N$ (8%) as well as the nature of chemical interactions between cellulose and hydroxyapatite after the grafting process. According to Figure 3, one single resonance peak of $^{31}P$ appears at 2.00 ppm for the nongrafted $HAP_N$ (Figure 3a), while after surface modification with 8 wt % of CMFs, the $^{31}P$ characteristic peak moves to 1.90 ppm as shown in Figure 3b, indicating that after surface modification, the chemical surrounding of the phosphorus atom in the $HAP_N$ crystal had been changed. Thus, these results are in good accordance with the previous data obtained by FTIR and XRD analysis and confirm the success of the grafting procedure of cellulose on the $HAP_N$ surface.

To determine the amount of cellulose polymer that had been grafted on the surface of $HAP_N$, the thermogravimetric analysis (TGA) was conducted. As shown in Figure 4a, the nongrafted $HAP_N$ displays little weight loss while the grafted one shows considerable weight loss due to the thermal decomposition of the cellulose polymer. At the same time, the grafting amount on $HAP_N$ modified with CMFs was found near to 8 wt %; this result further proved that the CMFs were successfully grafted onto the $HAP_N$ surface with the assumed amount.

To elucidate the morphological properties of the prepared $HAP_N$ and CMFs-*g*-$HAP_N$ (8%), scanning electron microscopy (SEM) analysis was carried out. As seen in Figure 5a,b, the surface of the $HAP_N$ is irregular in size, and the shapes and the agglomerates were arranged randomly with smooth and low visible porosity. However, the surface of the obtained powder after incorporation of CMFs (Figure 5c,d) is changed and seems to be rough due to the grafting of the cellulose polymer on the surface of $HAP_N$. This indicates that the $HAP_N$ particles are synthesized in situ on the surface of the cellulose to obtain the CMFs-*g*-$HAP_N$ (8%) thanks to a strong interaction between the cellulose and $HAP_N$ groups, and the prepared CMFs-*g*-$HAP_N$ (8%) is not result of a mechanical mixture of cellulose with $HAP_N$.

The nitrogen adsorption−desorption isotherms of $HAP_N$ and CMFs-*g*-$HAP_N$ (8%) (Figure 6a) display a characteristic type IV isotherm according to the IUPAC classification, indicating the presence of oval-shaped pores. The Barrett−Joyner−Halenda (BJH)-based pore size distributions (Figure 6b) of samples indicate that the pores are in the mesopore ranges (between 2 and 14 nm) with a central value of 2.53 and 2.91 nm respectively for $HAP_N$ and CMFs-*g*-$HAP_N$ (8%). Moreover, it can be noticed that the Brunauer−Emmett−Teller (BET) surface area of $HAP_N$ is 117.81 $m^2/g$, while the surface area of the CMFs-*g*-$HAP_N$ (8%) is 89.27 $m^2/g$. Thus, the grafting of cellulose microfibrils on the surface of $HAP_N$


https://doi.org/10.1021/acsomega.2c02108
ACS Omega 2022, 7, 28076−28092

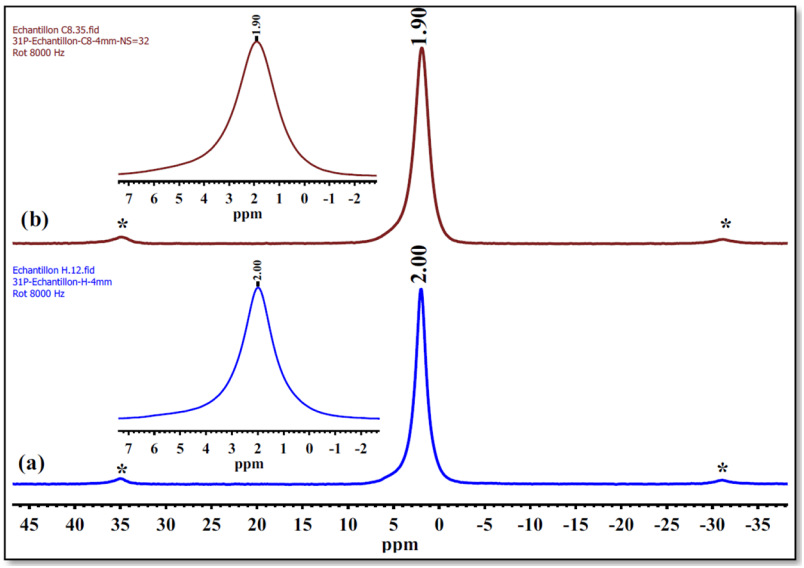


**Figure 3.** Solid-state $^{31}$P-MAS-NMR spectra of $HAP_N$ (a) and CMFs-*g*-$HAP_N$ (8%) (b).

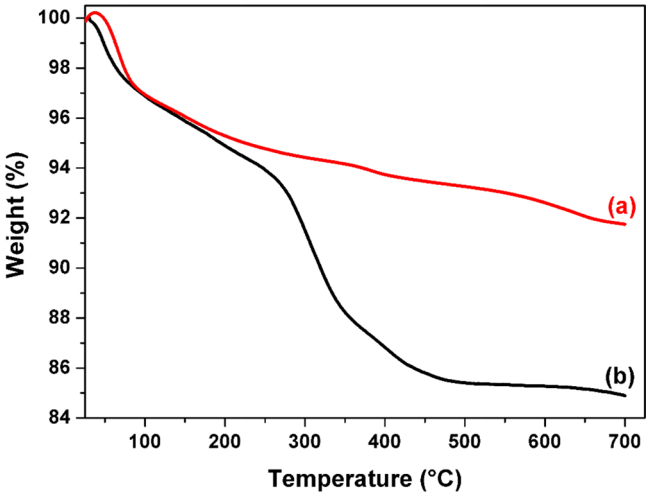


**Figure 4.** TGA curves of nongrafted $HAP_N$ (a) and CMFs-*g*-$HAP_N$ (8%) (b) powders.

could be the origin of this decrease in the surface area of CMFs-*g*-$HAP_N$ (8%) compared to that of $HAP_N$.

**2.2. Batch Adsorption Optimization Using RSM.** To evaluate the influence of operating parameters on the adsorption capacity of Pb(II) and Cu(II), three independent process variables were chosen: contact time ($X_1$), initial concentration of Pb(II), and Cu(II) ($X_2$) and CMFs-*g*-$HAP_N$ (8%) adsorbent amount ($X_3$). A total of 15 experiments have been executed in this work to investigate the effects of the three main independent factors on Pb(II) and Cu(II) adsorption capacity. The entire experimental design matrix for the three examined variables as well as the observed ($Y_1$, $Y_2$, $Y_3$, and $Y_4$) and the predicted ($\hat{Y}_1$, $\hat{Y}_2$, $\hat{Y}_3$, and $\hat{Y}_4$) responses of the Pb(II) and Cu(II) adsorption capacities (mg/g) and removal efficiencies (%) are provided in Table S1, Supporting Information.

The polynomial quadratic model was applied to figure out the interaction between independent and dependent variables. The predicted regression model for the two responses, namely, Pb(II) adsorption capacity ($\hat{Y}_1$, mg/g) and Cu(II) adsorption capacity ($\hat{Y}_2$, mg/g) can be expressed as follows:

$$\hat{Y}_1 = 52.397 + 1.126\,X_1 + 13.436\,X_2 - 28.310\,X_3 - 0.217\,X_1^2 + 4.673\,X_2^2 + 11.745\,X_3^2 - 0.902\,X_1X_2 - 0.645\,X_1X_3 - 7.980\,X_2X_3 \quad (1)$$

$$\hat{Y}_2 = 35.973 + 0.078X_1 + 5.205\,X_2 - 5.292\,X_3 - 7.707\,X_1^2 + 1.433\,X_2^2 + 0.253\,X_3^2 - 1.520\,X_1X_2 + 1.790\,X_1X_3 - 9.070\,X_2X_3 \quad (2)$$

The significance of the polynomial quadratic model was analyzed and validated using the analysis of variance (ANOVA). The ANOVA results of Pb(II) and Cu(II) adsorption capacities are presented in Table 1 while those of Pb(II) and Cu(II) removal efficiencies are given in Table S2, Supporting Information. The statistical significance of the model is checked by its *P*-value and *F*-value, in which the *p*-value less than 5% is recognized statistically significant.[39]

The ANOVA indicates that the second-order polynomial model was statistically significant and adequate to represent the actual relationship between the response and the independent variables, with a very small *p*-value (0.01 and 2.26% for Pb(II) and Cu(II), respectively). This implies that the suggested model describes the experimental data well, with an insignificant lack of fit (*p*-value >5%).[39]

Furthermore, the significance of all linear terms ($X_1$, $X_2$, and $X_3$), interaction terms ($X_1X_2$, $X_1X_3$, and $X_2X_3$), and quadratic terms ( $X_1^2$, $X_2^2$, and $X_3^2$) on the response variations was evaluated by *p*-values as shown in Table S3. Indeed, in the case of Pb(II) removal, initial Pb(II) concentration ($X_2$), the adsorbent amount ($X_3$), and their interactive term ($X_2X_3$) as well as the quadratic terms ($X^2_3$) and ($X^2_2$) have a *P*-value less than 5% and therefore are considered as potentially significant coefficients. As for the Cu(II) removal, initial Cu(II) concentration ($X_2$), the adsorbent amount ($X_3$), and the quadratic term ($X^2_1$) as well as the interactive term ($X_2X_3$) show a *p*-value inferior to 5% and therefore are selected as potentially significant coefficients.


https://doi.org/10.1021/acsomega.2c02108
ACS Omega 2022, 7, 28076−28092

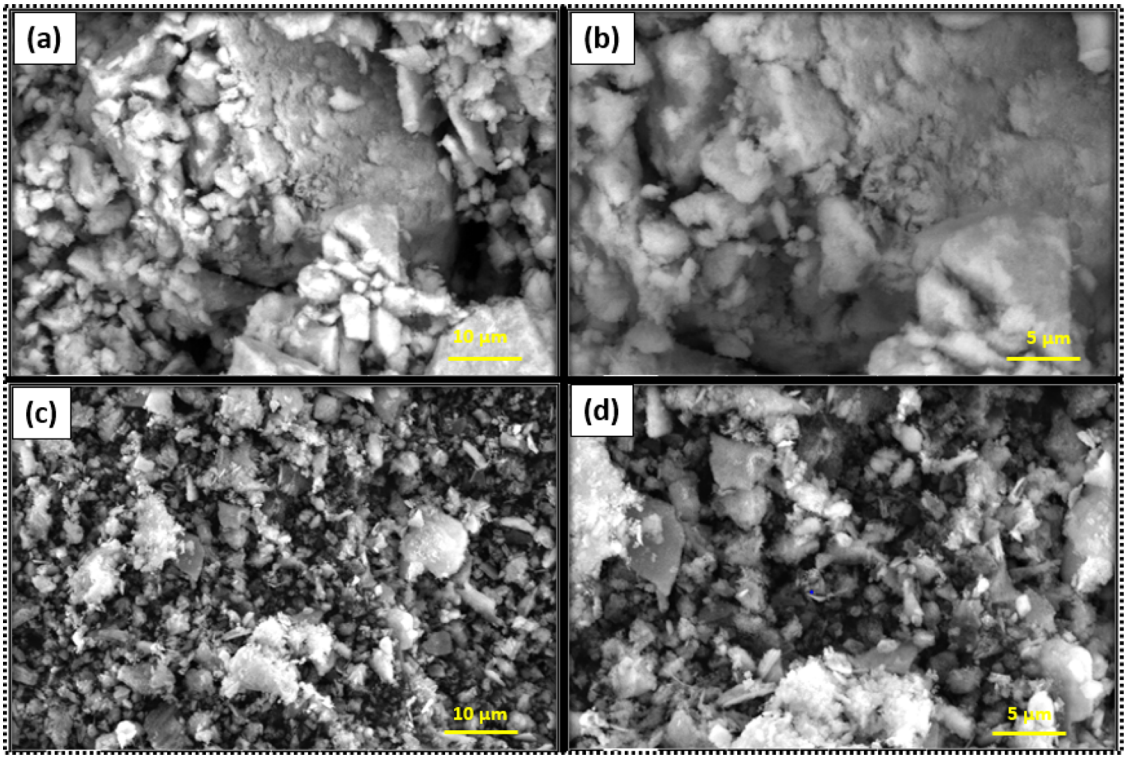


**Figure 5.** SEM micrograph of $HAP_N$ (a and b) and CMFs-*g*-$HAP_N$ (8%) (c and d).

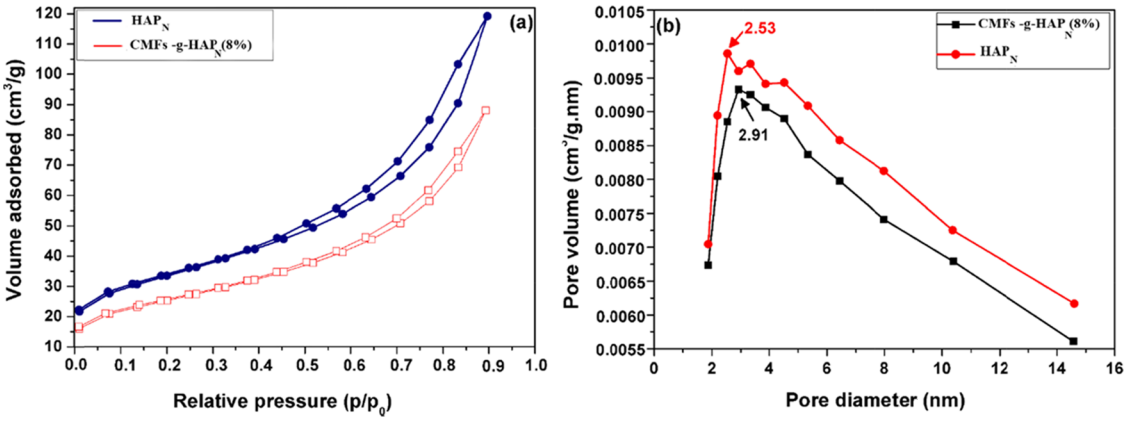


**Figure 6.** Nitrogen adsorption−desorption isotherm and BJH pore size distribution of (a) $HAP_N$ and (b) CMFs-*g*-$HAP_N$ (8%).

**Table 1. ANOVA of Pb(II) and Cu(II) Adsorption Capacity (mg/g)**

| metal ion | source | sum of squares | $D_f$ | mean square | *F*-value | *p*-value (%) |
|---|---|---|---|---|---|---|
| Pb(II) | regression | 8695.060 | 9 | 966.118 | 147.534 | <0.01*** |
| | residual | 32.742 | 5 | 6.548 | | |
| | lack of fit | 30.359 | 3 | 10.119 | 8.4938 | 10.7 |
| | pure error | 2.3828 | 2 | 1.191 | | |
| Cu(II) | regression | 1028.370 | 9 | 114.263 | 6.9996 | 2.26* |
| | residual | 81.620 | 5 | 16.324 | | |
| | lack of fit | 75.699 | 3 | 25.233 | 8.5232 | 10.7 |
| | pure error | 5.921 | 2 | 2.960 | | |

The values marked with one asterisk are significant and those with three asterisks are more significant.

Based on the statistical analysis of regression coefficients (as listed in Table S3, Supporting Information), the results indicated that the most significant coefficients, which have a synergetic effect on Pb(II) adsorption efficiency, are the linear term $X_2$ and the quadratic terms $X^2_2$ and $X^2_3$, while the linear term $X_3$, the quadratic term $X^2_1$, and the interaction term ($X_2X_3$) indicate that these coefficients have an antagonist effect on the response (adsorption capacity). In the case of the Cu(II) adsorption process, the linear term $X_2$ showed a synergetic influence on response variations, while other



https://doi.org/10.1021/acsomega.2c02108
ACS Omega 2022, 7, 28076−28092

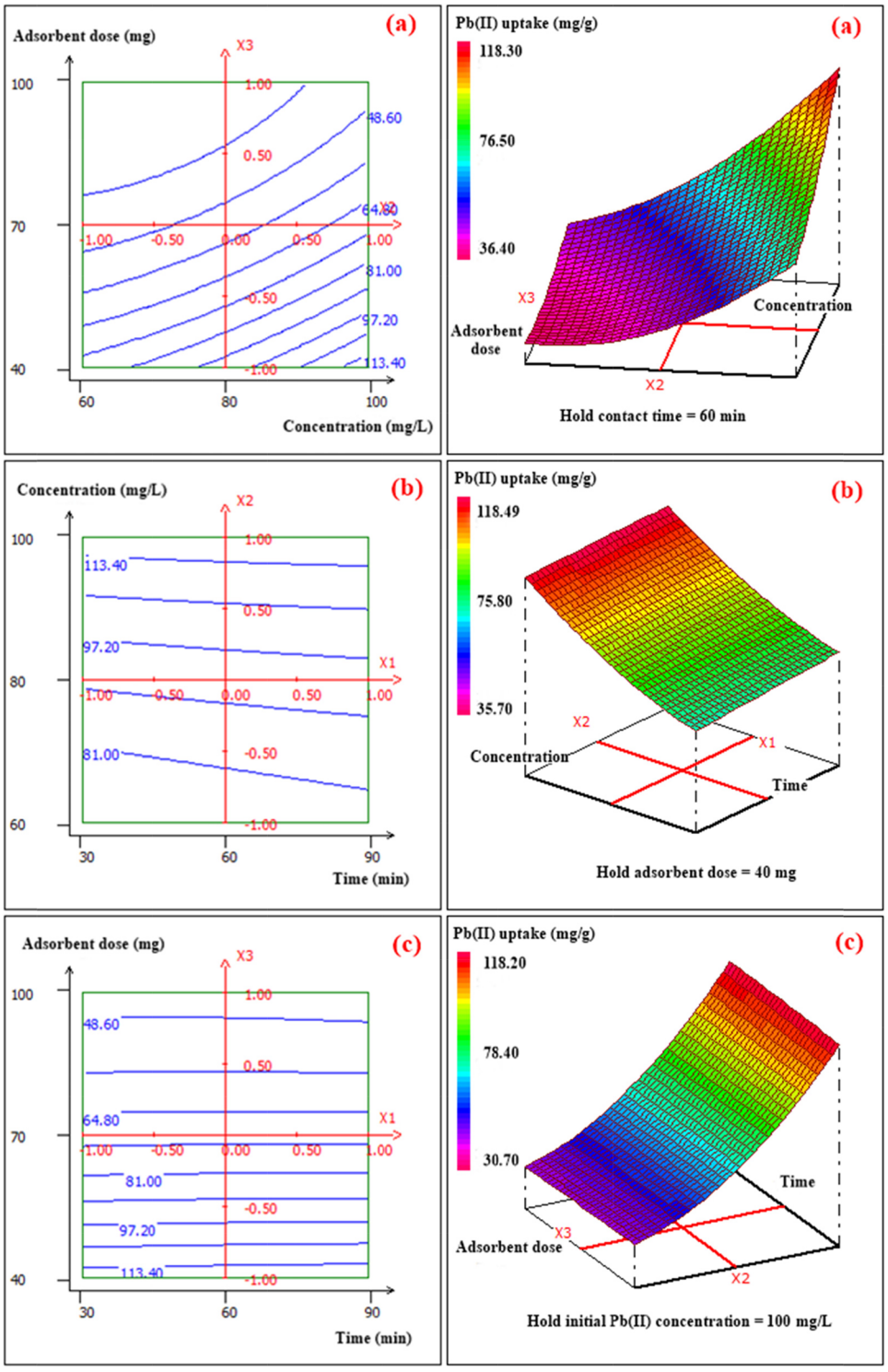


**Figure 7.** 2D-3D surface plots of the effect of adsorbent dose and initial Pb(II) concentration (a), contact time and initial Pb(II) concentration (b), and adsorbent dose and contact time (c) on Pb(II) adsorption capacity (mg/g).

coefficients including the linear term $X_3$, the quadratic term $X^2_{1,}$ and the interaction term $X_2X_3$ exhibited an antagonist influence on Cu(II) adsorption capacity variations.

The 2D and 3D plots displaying the influences of the independent variables and their interactions on the response are presented in Figures 7 and 8 for Pb(II) and Cu(II) adsorption capacities (mg/g), respectively. It can be noticed that the adsorption capacity of Pb(II) is highly affected by the initial concentration (Figure 7a) while the contact time has no significant effect on the response variation (Figure 7c). Also, it can be observed from Figure 8a that the adsorption capacity of Cu(II) is highly affected by the initial concentration and adsorbent dose. In accordance with these plots, the optimum predicted conditions for maximum adsorption capacities of Pb(II) and Cu(II) are presented in Table 2, respectively. As can be seen from this table, the output results from the model indicated good agreement between the experimental and predicted values of adsorption capacity (mg/g). This close


https://doi.org/10.1021/acsomega.2c02108
ACS Omega 2022, 7, 28076−28092

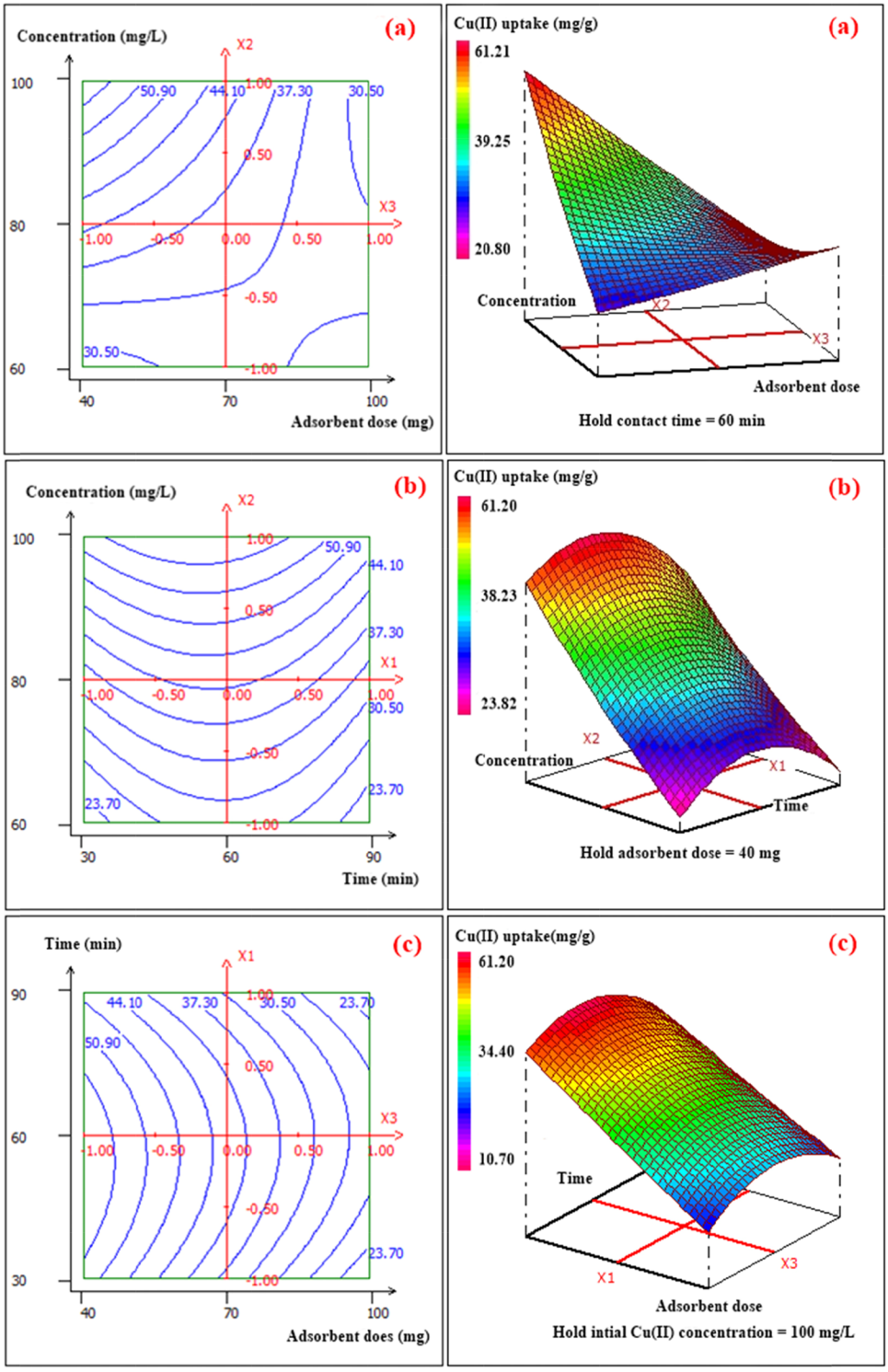


**Figure 8.** 2D-3D surface graphs of the effect of (a) initial Cu(II) concentration and adsorbent dose, (b) contact time and initial Cu(II) concentration, and (c) adsorbent dose and contact time on Cu(II) adsorption capacity (mg/g).

**Table 2. Predicted and Experimental Adsorption Capacities of Pb(II) and Cu(II)**

| factor | predicted adsorption capacities (mg/g) | | experimental adsorption capacities (mg/g) | |
|---|---|---|---|---|
| | Pb(II) | Cu(II) | Pb(II) | Cu(II) |
| contact time = 60 min<br>initial concentration = 100 mg/L<br>adsorbent dose = 40 mg | 118.49 ± 2.55 | 61.21 ± 4.04 | 120.74 ± 2.13 | 58.83 ± 3.06 |



https://doi.org/10.1021/acsomega.2c02108
ACS Omega 2022, 7, 28076−28092

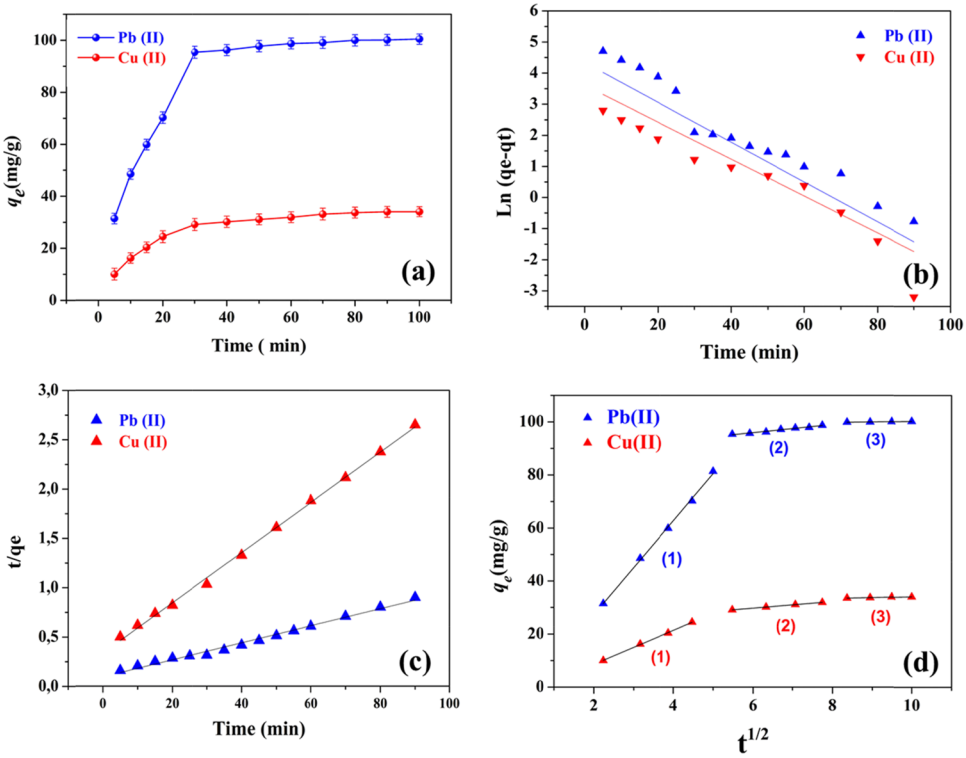


**Figure 9.** (a) Effect of contact time on the Pb(II) and Cu(II) adsorption capacity (mg/g), (b) pseudo-first-order, (c) pseudo-second-order kinetic, and (d) intraparticle diffusion kinetic models.

**Table 3. Kinetic Parameters for the Adsorption of Pb(II) and Cu(II) by CMFs-*g*-HAP$_N$ (8%)**

| metal | pseudo-first order | | | pseudo-second order | | |
|---|---|---|---|---|---|---|
| | $q_e$ (mg/g) | $K_1$ (1/min) | $R^2$ | $q_e$ (mg/g) | $K_2$ (g/mg min) | $R^2$ |
| Pb(II) | 76.77 | 0.06402 | 0.95 | 116.14 | 0.00077 | 0.98 |
| Cu(II) | 36.98 | 0.05938 | 0.92 | 39.24 | 0.00194 | 0.99 |

correlation between the experimental and predicted values was also proven by the values of $R^2$ (0.998 and 0.926 for Pb(II) and Cu(II), respectively) and adjusted $R^2$ (0.989 and 0.794 for Pb(II) and Cu(II), respectively) as shown in Figure S1, Supporting Information, which are found to be close to one. Consequently, these optimal operational parameters were then used to study kinetics, adsorption isotherms, and thermodynamics.

**2.3. Adsorption Kinetic Studies.** The contact time between the adsorbent and adsorbate during the adsorption process is one of the economic factors that has great importance for an industrial application because it significantly affects the efficiency of the adsorption process.[51] The results of the experiments performed to determine the contact time effect on the adsorption of Pb(II) and Cu(II) metals onto CMFs-*g*-HAP$_N$ (8%) are given in Figure 9a. The initial concentration and adsorbent amount for the experimental conditions of the adsorption process were determined as 80 mg/L and 40 mg, respectively. It can be seen from Figure 9a that the adsorption capacity of both metals was increased very rapidly during the first 30 min, and then it slowly increased and reached the equilibrium point around 60 min for both metals. This can be explained by the presence of a large number of active sites in the empty adsorbent surface before the metal uptake. After increasing the contact time, a decrease occurred in the available adsorption regions, thus limiting the adsorbent−adsorbate interactions. It was also noticed that the absorption of Pb(II) in the whole process was stronger and faster than that of Cu(II), suggesting a relatively higher affinity between Pb(II) and CMFs-*g*-HAP$_N$ (8%) adsorbent.[52] The maximum Pb(II) adsorption capacity of CMFs-*g*-HAP$_N$ (8%) (120 mg/g) over a time period of 60 min is quite higher than that of carbonate hydroxyapatite extracted from eggshells waste (CHAP) over a time period of 200 min.[53]

To deeply explain the control mechanism of the adsorption process of Pb(II) and Cu(II) onto CMFs-*g*-HAP$_N$ (8%), the mass transfer, and chemical reaction, the pseudo-first-order and pseudo-second-order models were applied (Figure 9b,c). The experimental data and their linear forms are described using the following equations:[39]

$$\ln(q_e - q_t) = \ln q_e - K_1 t \tag{3}$$

$$\frac{t}{q_t} = \frac{1}{K_2 q_e^2} + \frac{t}{q_e} \tag{4}$$

where $q_e$ (mg/g) is the adsorption capacity of the metal ion at the equilibrium, $q_t$ (mg/g) is the adsorption capacity of the metal ion at $t$ time, $K_1$ (min$^{-1}$) is the pseudo-first-order kinetic model rate constant, and $K_2$ (g/mg min) is the pseudo-second-order kinetic model rate constant.

Based on the obtained model parameter values presented in Table 3, the correlation coefficient values ($R^2$ = 0.98 for Pb(II)



https://doi.org/10.1021/acsomega.2c02108
ACS Omega 2022, 7, 28076−28092

and $R^2$ = 0.99 for Cu(II)) of the pseudo-second-order model were higher than those of the pseudo-first-order model ($R^2$ = 0.95 for Pb(II) and $R^2$ = 0.92 for Cu(II)). Hence, the adsorption behavior of Pb(II) and Cu(II) can be well described by the pseudo-second-order model where the efficiency of Pb(II) and Cu(II) adsorption heavily relies on the number of available active sites of the CMFs-*g*-$HAP_N$ (8%) adsorbent.[52]

To identify the diffusion mechanism of Pb(II) and Cu(II) adsorption onto CMFs-*g*-$HAP_N$ (8%), the intraparticle diffusion model has also been applied. The intraparticle diffusion model is represented as:

$$q_t = K_i t^{1/2} - C_i \quad (5)$$

where $K_i$ is the intraparticle diffusion rate constant (g $mg^{-1}$ $min^{-1/2}$) and $C_i$ is a constant associated with the degree of the interface effect. It supplies information on the resistance to external mass transfer and the width of the boundary film.[39]

As can be seen from Figure 9d, the adsorption process of both metals onto CMFs-*g*-$HAP_N$ (8%) occurred in three distinct stages represented by three distinct linear plots. The rate constant $K_i$ for each step is estimated directly from the slope of the regression curve (Table 4). The first initial linear section corresponds to the diffusion of the metal ions from the bulk solution to the CMFs-*g*-$HAP_N$ (8%) surface followed by a second stage representing intraparticle diffusion into the branched porous network of the adsorbent. The third one is the equilibrium stage. From Table 4, the high values of $R^2$ obtained for both metal ions showed that the intraparticle diffusion mechanism played an important role in the sorption process mechanism.

**Table 4. Intraparticle Diffusion Kinetic Parameters for the Adsorption of Pb(II) and Cu(II) by CMFs-*g*-$HAP_N$ (8%)**

| metallic ion | parameter | step 1 | step 2 | step 3 |
|---|---|---|---|---|
| Pb(II) | $K_1$ (g $mg^{-1}$ $min^{-1/2}$) | 17.72 | 1.5324 | 0.21445 |
| | $C_1$ (mg/g) | −8.17471 | 86.75123 | 98.0742 |
| | $R^2$ | 0.99 | 0.97 | 0.94 |
| Cu(II) | $K_2$ (g $mg^{-1}$ $min^{-1/2}$) | 6.38659 | 1.2452 | 0.33689 |
| | $C_2$ (mg/g) | −4.17596 | 22.2582 | 30.69827 |
| | $R^2$ | 0.99 | 0.99 | 0.92 |

**2.4. Adsorption Isotherms.** Adsorption isotherms are of great importance to analyze properly the interaction nature between the adsorbent and adsorbate once the adsorption process reaches equilibrium. These often reveal the distribution of available adsorption sites on the surface of the adsorbent and contribute to the understanding of the adsorption mechanism.[35]

As a first step and in order to study the effect of the initial Pb(II) and Cu(II) concentrations on the adsorption efficiency and to better understand the uptake patterns, adsorption experiments were performed by varying the concentration of the initial metal from 50 to 400 mg/L. In these experiments, the contact time and the adsorbent content were maintained at 60 min and 40 mg, respectively. The impact of the initial metal concentration on the adsorption capacity (mg/g) under the previous operating conditions is presented in Figure 10a.

As can be observed from this figure, the adsorption capacity of both metals increases with the initial concentration and eventually reaches saturation. Higher Pb(II) and Cu(II) concentrations result in a greater driving force for the mass transfer from the batch solution to the adsorbent interface, leading to a faster adsorption increasing the adsorption capacity. Moreover, as the metal concentrations increase, the adsorption sites get saturated. It is also noticed that uptake of Pb(II) is higher than that of Cu(II), suggesting again that the interaction between CMFs-*g*-$HAP_N$ (8%) and Pb(II) is stronger than that of Cu(II).

Out of the different adsorption isotherms, the Langmuir and Freundlich isotherms are the most widely employed for the adsorption of heavy metals. Thus, in this part of the study Langmuir and Freundlich isotherms were used to describe the interactions between the metal ions and the CMFs-*g*-$HAP_N$ (8%) surface during the adsorption process. The Langmuir adsorption model is focused on the assumption that the maximum adsorption corresponds to a saturated monolayer of dissolved solute molecules on the adsorbent surface. The expression of the Langmuir model with the linear equation is given below in eq 6:

$$\frac{C_e}{q_e} = \frac{1}{q_m K_L} + \frac{C_e}{q_m} \quad (6)$$

where $C_e$ (mg/L) is the metal ion concentration in solution at equilibrium, $q_e$ (mg/g) is the amount of adsorbed metal ion per unit mass of sorbent, $q_m$ (mg/g) is the maximum amount of the adsorbed metal ion per unit mass of adsorbent (monolayer), and $K_L$(L/mg) is a constant relative to the affinity of the binding sites.

The Freundlich model accepts heterogeneous adsorption according to the variety of adsorption zones, and its linear equation is given below:

$$\mathrm{Ln}(q_e) = \ln(K_F) + \frac{1}{n}\ln C_e \quad (7)$$

According to the data reported in Table 5 based on the evaluated correlation coefficients ($R^2$), it can be said that the adsorption of both metals fitted better to the Langmuir isotherm model (0.99 for Pb(II) and 0.98 for Cu(II)) compared with the Freundlich isotherm model (0.86 for Pb(II) and 0.57 for Cu(II)). Moreover, the Langmuir isotherm model assumes that a monolayer adsorption occurs onto a solid surface with a definite number of identical sites and there is no interaction between the metal ions.[35] The linear plot of the Langmuir model for the adsorption of Pb(II) and Cu(II) onto CMFs-*g*-$HAP_N$ (8%) is given in Figure 10b.

Because the nature of the sorption mechanisms cannot be determined by using the Langmuir and Freundlich isotherm models, the Dubinin−Radushkevich model, which gives a more accurate view of the nature of the sorption process, was used. The model equation is expressed as follows:

$$E_a = \frac{1}{\sqrt{2\beta}} \quad (8)$$

The value of $E_a$ is used to estimate the nature of the sorption process; if this value is in the range of 8 to 16 kJ/mol, the sorption type is chemisorption, while values below 8 kJ/mol indicate the physical nature of sorption. According to the D-R model and the obtained $E_a$ values (Table 6), Pb(II) and Cu(II) sorption onto CMFs-*g*-$HAP_N$ (8%) proved to be dominantly by physical nature rather than chemical sorption.

**2.5. Thermodynamic Parameters of the Adsorption Process.** The effect of temperature on the adsorption of the


https://doi.org/10.1021/acsomega.2c02108
ACS Omega 2022, 7, 28076−28092

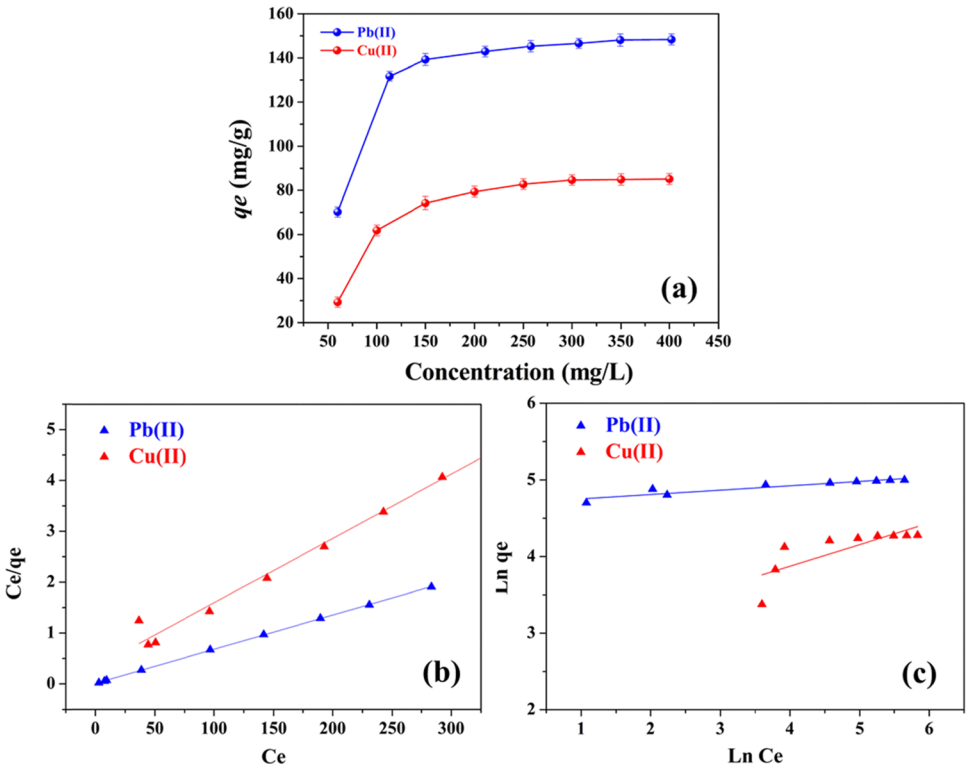


**Figure 10.** (a) Effect of initial Pb(II) and Cu(II) concentrations on the adsorption capacity and linear fitting plots of (b) Langmuir and (c) Freundlich isotherms.

**Table 5. Isotherm Parameters for Pb(II) and Cu(II) and Adsorption onto CMFs-*g*-HAP$_N$ (8%)**

| isotherm | parameters | Pb(II) | Cu(II) |
|---|---|---|---|
| Langmuir | $q_{max}$ (mg/g) | 148.80 | 87.05 |
| | $K_L$ (L min$^{-1}$) | 0.45683 | 0.0377 |
| | $R^2$ | 0.99 | 0.98 |
| Freundlich | $K_F$ | 109.45 | 15.54 |
| | $1/n$ | 0.05704 | 0.2825 |
| | $R^2$ | 0.86 | 0.57 |

**Table 6. Sorption Energy Values, $E_a$, of Pb(II) and Cu(II) onto CMFs-*g*-HAP$_N$ (8%)**

| | $E_a$ (kJ/mol) | |
|---|---|---|
| sorbent | Pb(II) | Cu(II) |
| CMFs-g-HAP$_N$ (8%) | 1.839 | 0.048 |

Pb(II) and Cu(II) metal ions was investigated in the 298−338 K temperature range in order to determine the thermodynamic parameters, namely, $\Delta G^\circ$, $\Delta H^\circ$, and $\Delta S^\circ$. These parameters are calculated utilizing the equations given below (eqs 9−11).

$$\Delta G^\circ = -RT\ln K \tag{9}$$

$$\ln K = \frac{\Delta S^\circ}{R} - \frac{\Delta H^\circ}{RT} \tag{10}$$

$$\Delta G^\circ = \Delta H^\circ - T\Delta S^\circ \tag{11}$$

where $\Delta G^\circ$ (kJ/mol) is Gibbs free energy, $\Delta H^\circ$ (kJ/mol) is enthalpy, $\Delta S^\circ$ (J/mol K) is entropy, $R$ (8.314 J/mo1 K) is the ideal gas constant, and $T$ is the temperature.

$\Delta H^\circ$ and $\Delta S^\circ$ can be calculated from the slope and intercept by the linear plot of ln$K$ vs $1/T$. As can be seen from Table 7, the negative $\Delta G^\circ$ values for the adsorption of both metals indicated the spontaneous nature of the adsorption process. While the positive value of $\Delta S^\circ$ demonstrated a good affinity between the Pb(II) and Cu(II) ions accordingly and the

**Table 7. Thermodynamic Parameters for the Adsorption of Pb(II) and Cu(II) on the CMFs-*g*-HAP$_N$ (8%)**

| metallic ion | $T^\circ$ (K) | $\Delta G^\circ$ (kJ mol$^{-1}$) | $\Delta S^\circ$ (kJ mol$^{-1}$ K$^{-1}$) | $\Delta H^\circ$ (kJ mol$^{-1}$) |
|---|---|---|---|---|
| Pb(II) | 298.11 | −27.86 | 0.078 | −4.37 |
| | 308.85 | −28.55 | | |
| | 318.45 | −29.07 | | |
| | 328.15 | −30.23 | | |
| | 338.65 | −30.74 | | |
| Cu(II) | 298.17 | −25.17 | 0.047 | −11.06 |
| | 308.15 | −25.45 | | |
| | 318.33 | −26.12 | | |
| | 328.25 | −26.53 | | |
| | 338.24 | −27.06 | | |



https://doi.org/10.1021/acsomega.2c02108
ACS Omega 2022, 7, 28076−28092

surface of the CMFs-*g*-HAP$_N$ (8%) adsorbent, the disorder at the solid−solution interface took place during the adsorption process. In addition, the negative values of $\Delta H^\circ$ supported the exothermic adsorption reaction.

**2.6. Desorption and Regeneration of CMFs-*g*-HAP$_N$ (8%).** Desorption is the most significant aspect of the adsorption treatment technique, especially in industrial applications; it reflects the reusability of the adsorbent material. Within this context, batch desorption experiments were carried out using a solution of different eluents EDTA-Na$_2$ (0.01 M), oxalic acid (0.01 M), NaOH (0.1 M), and ethanol (0.1 M), under the same conditions. Figure 11 shows

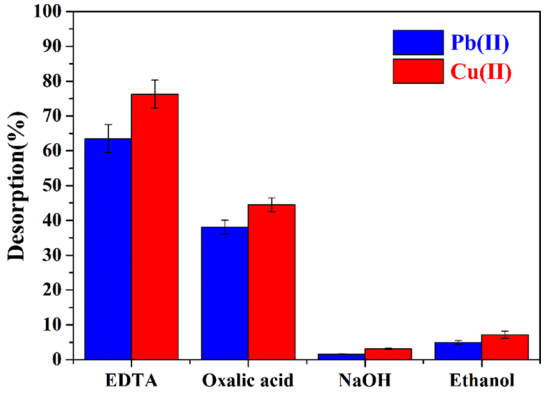


**Figure 11.** Desorption of Pb(II) and Cu(II) from CMFs-*g*-HAP$_N$ (8%) using various eluents.

the screening study of different eluent agents on the desorption efficiencies. Based on the obtained results, EDTA-Na$_2$ showed the highest desorption percentage (65% for Pb(II) and 73% for Cu(II)). This can be explained by a complex formation between EDTA-Na$_2$ and the metal ions present in the solution.[28] Additionally, the desorption efficiency was reduced to 60% for Pb(II) and 66% for Cu(II)) when using oxalic acid, while the use of NaOH and ethanol resulted in very low desorption and has not exceeded 10% for both metals. Another noteworthy result is that, regardless of the eluent used, the desorption of Pb(II) remains lower than that of Cu(II), which again confirms its relatively higher affinity with CMFs-*g*-HAP$_N$ (8%). The reusability of the prepared adsorbent can be explained by its stability and constancy after the Pb(II) and Cu(II) adsorption process; as can be seen clearly in Figures S2 and S3 (Supporting Information) no remarkable changes have occurred in the CMFs-*g*-HAP$_N$ (8%) structure.

The recovery test was repeated for three cycles, and the results are illustrated in Figure 12. As shown, the adsorption efficiency of CMFs-*g*-HAP$_N$ (8%) decreases for every new cycle. The maximum adsorption efficiency of CMFs-*g*-HAP$_N$ (8%) for Pb(II) and Cu(II) was found to be 99.7 and 98%, respectively. After three cycles, the adsorption efficiency dropped to 55% for Pb(II) and 60% for Cu(II). These promising results indicated that CMFs-*g*-HAP$_N$ (8%) could be regenerated and repeatedly used in heavy metal removal.

**2.7. Effect of Coexisting Cations.** In view of the complexity of wastewater constitution, the existence of other cations in wastewater may affect the performance of the adsorbent for heavy metal ion removal.[53] Therefore, lead and copper sorption using CMFs-*g*-HAP$_N$ (8%) in the presence of common coexisting cations including monovalent ($Na^+$) cation and divalent ($Ca^{2+}$, $Mg^{2+}$) cations was investigated in single

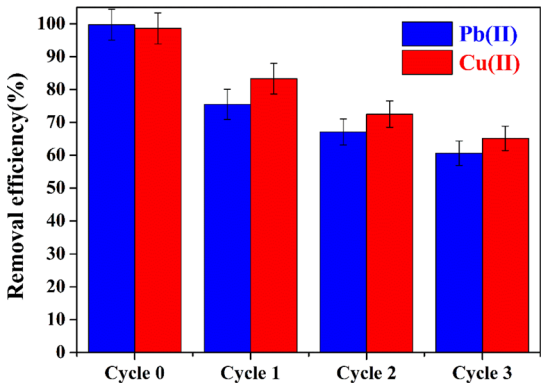


**Figure 12.** Effect of recovery cycles on the removal efficiency of Pb(II) and Cu(II) onto CMFs-*g*-HAP$_N$ (8%).

and binary systems. As can be seen from Figure 13a,b, the adsorption capacity of CMFs-*g*-HAP$_N$ (8%) as well as its

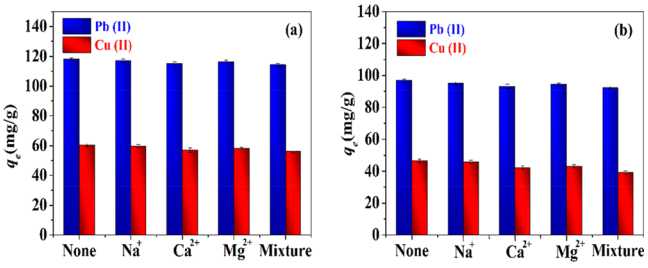


**Figure 13.** Effect of coexisting cations on Pb(II) and Cu(II) removal onto CMFs-*g*-HAP$_N$ (8%) in (a) single system and (b) binary system.

selectivity toward the studied metals was slightly or non-significantly affected by the presence of $Na^+$, $Mg^{2+}$ and $Ca^{2+}$ cations. Furthermore, it should be noted that the lowest decrease in Cu(II) and Pb(II) uptake that was observed in the solution mixture (all CIs) did not exceed 5%, which leads to the conclusion that the CMFs-*g*-HAP$_N$ (8%) adsorbent could selectively and efficiently remove Pb(II) and Cu(II) ions from polluted water containing coexisting cations.

However, it was noticed that the competitive sorption among Pb(II) and Cu(II) using CMFs-*g*-HAP$_N$ (8%) in the binary system has been significantly affected, where the adsorption capacity of Pb(II) and Cu(II) decreased by 18% (from 118 to 96 mg/g) and 22% (from 60 to 46 mg/g), respectively. The higher affinity of the prepared adsorbent for Pb ions could be due to the higher Pauling electronegativity of Pb (2.33) compared to Cu (1.90), which favors electrostatic complexation and inner sphere surface interactions.[53−55]

**2.8. Adsorption Mechanism.** The adsorption mechanism of a metal into an adsorbent depends on various factors including the properties of the adsorbent, the nature of the adsorbate, and the likely interactions between the adsorbate and the adsorbent.[39] The apatite materials including HAP$_N$ have a large specific surface area and also contain the surface groups such as $PO_4^{3-}$, $Ca^{2+}$, and $OH^-$; they have a significant electrostatic adsorption of macromolecules, small molecules, and ion exchange capacity.[56]

As discussed above and based on the XRD and FTIR results of the recovered adsorbents (Figures S3 and S4 in the Supporting Information), we can reasonably conclude that the removal of Pb(II) and Cu(II) by CMFs-*g*-HAP$_N$ (8%) might be governed by physical rather than chemical mechanisms via


https://doi.org/10.1021/acsomega.2c02108
ACS Omega 2022, 7, 28076−28092

surface complexation, electrostatic interaction, and ion exchange;[50] this is further confirmed with the fact that the CMFs-*g*-$HAP_N$ (8%) adsorbent is favorably regenerated with the complexing agent EDTA-$Na_2$. Similar conclusions have also been reported by Yan et al.[28] for the removal of Pb(II) and Cd(II) from wastewater. Herein, the complexation mechanism may contribute to Pb(II) and Cu(II) binding through the exchange of these ions with $H^+$ from hydroxyl groups of CMFs-*g*-$HAP_N$ (8%).[50] In addition, the CMF abundant hydroxyl groups could act as active sites for metal removal and thus bind with these ions via electrostatic interactions.[57]

In the other hand, a test was conducted in order to verify the implication of the ion exchange mechanism in the adsorption process; the $Ca^{2+}$ concentration in the bulk solution was also measured before and after Pb(II) and Cu(II) adsorption onto CMFs-*g*-$HAP_N$ (8%). Indeed, this test indicated that these two metals were partially exchanged with the $Ca^{2+}$ ions during the adsorption process. In view of these findings, a scheme was proposed to illustrate the mechanism of Pb(II) and Cu(II) adsorption onto CMFs-*g*-$HAP_N$ (8%) (Scheme 1).

**Scheme 1. Suggested Mechanism of Pb(II) and Cu(II) Adsorption onto CMFs-*g*-$HAP_N$ (8%)**

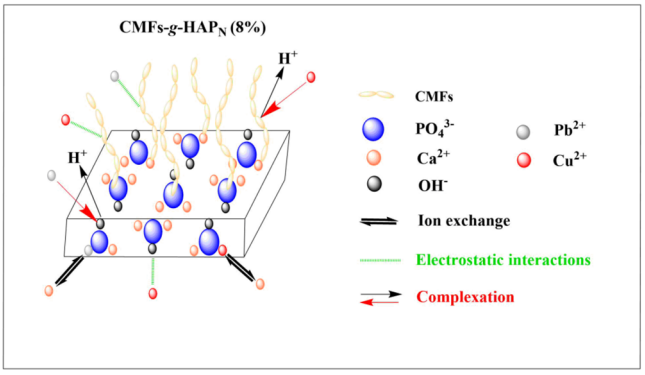


**2.9. Comparison with Other Adsorbents.** In accordance with the literature, numerous adsorbents have been studied for Pb(II) and Cu(II) removal from aqueous solution. The efficiency of our adsorbent was investigated against the other reported adsorbents as illustrated in Table 8. As listed in Table 8, the proposed adsorbent exhibited higher adsorption affinity toward Pb(II) and Cu(II) with respect to the other adsorbents. Hence, the prepared CMFs-*g*-$HAP_N$ (8%) is extremely recommended as an efficient adsorbent given its eco-friendliness, low cost, and high adsorption efficiency for heavy metal removal.

**Table 8. Comparison of Different Adsorbents for Pb(II) and Cu(II) Adsorption**

| metals | adsorbent | $q_m$ (mg/g) | removal (%) | ref |
|---|---|---|---|---|
| Pb(II) | CMFs-*g*-$HAP_N$ (8%) | 148.80 | 99.7 | this study |
| | natural clay | 25.07 | 62.41 | 58 |
| | carbonate hydroxyapatite | 126.1 | 92.35 | 53 |
| | magnetic cellulose acetate | 44.5 | 98.4 | 59 |
| | HAP/chitosan nanostructures | 196.2 | 99.9 | 60 |
| | sludge biochar | 51.20 | 99 | 61 |
| Cu(II) | CMFs-*g*-$HAP_N$ (8%) | 87.05 | 98.6 | this study |
| | CMC-Alg/GO | 64 | 90 | 35 |
| | polyaniline/clay nanomaterials | 22.77 | | 62 |
| | hydroxyapatite/biochar | 99.01 | 99 | 3 |
| | DTPA-chitosan/alginate beads | 107.1 | 93 | 63 |

## 3. CONCLUSIONS

In this study, a novel and easy approach has been proposed to prepare in situ CMFs-*g*-$HAP_N$ (8%) using phosphate rock and date palm petiole as alternative and natural Moroccan resources. The prepared sample was successfully characterized by various physicochemical techniques in order to study its structural, textural, and morphological properties. Then, the statistical methodology, Box–Behnken response surface design was demonstrated to be effective and reliable in finding the optimal conditions for the adsorption of Pb(II) and Cu(II) onto CMFs-*g*-$HAP_N$ (8%) from an aqueous solution. The results showed that the adsorption conditions have significant effects on the removal of Pb(II) and Cu(II) ions. The response surface plots were used for estimating the interactive effect of three independent variables (initial metal ion concentration, contact time, and adsorbent dose) on the response (adsorption capacity of heavy metals). The second-order mathematical model was developed by regression analysis of the experimental data obtained from 15 batch runs. The optimal conditions for 118.49 ± 2.55 and 61.21 ± 4.04 mg/g of Pb(II) and Cu(II) removal, respectively, were predicted to be 40 mg of CMFs-*g*-$HAP_N$ (8%), a metal initial concentration of 100 mg $L^{-1}$, and a contact time of 60 min. The pseudo-second-order model was found to be the applicable kinetic model in the present study. The Langmuir and Freundlich isotherm models were used for the description of the adsorption equilibrium of Pb(II) and Cu(II). The data were in good agreement with the Langmuir isotherm. Furthermore, this study demonstrated that the CMFs-*g*-$HAP_N$ (8%) has relatively high adsorption capacity compared to some other adsorbents reported in the literature. For practical application, the CMFs-*g*-$HAP_N$ (8%) adsorbent appeared to be a promising candidate to replace the conventional and expensive adsorbents, currently used in the removal of heavy metals from the aqueous solution.

## 4. EXPERIMENTAL SECTION

**4.1. Materials.** Natural phosphate (NP) sample originated from Khouribga region (Morocco) was used as a source of calcium and phosphate precursor ions in view to prepare natural hydroxyapatite ($HAP_N$). The natural fibers used in this work are date palm fibers (DPFs) collected from the region of Errachidia in southeast of Morocco. Lead nitrate ($Pb(NO_3)_2$) and copper sulfate ($CuSO_4{,}5H_2O$) were of analytical grade and were supplied by VWR international PROLABO. Ethylenediaminetetraacetic acid disodium salt dihydrate (EDTA-$Na_2$), sodium hydroxide (NaOH), and sodium hypochlorite (NaClO) were purchased from Sigma-Aldrich. The precursor salts of NaCl, $CaCl_2$, and $MgSO_4$ (used for coexisting ions) were of analytical grade and purchased from Sigma-Aldrich. Distilled water was used throughout experiments.

**4.2. Preparation of Cellulose Microfibrils.** The cellulose fibers were prepared as described in detail in our previous report.[64] First, the raw DPF was ground and sieved using a 500 $\mu$m sieve to eliminate small particles and fine powders.


https://doi.org/10.1021/acsomega.2c02108
ACS Omega 2022, 7, 28076−28092

Scheme 2. Schematic Illustration of the Preparation Process of CMFs-*g*-$HAP_N$ (8%) from Natural Phosphate and CMFs

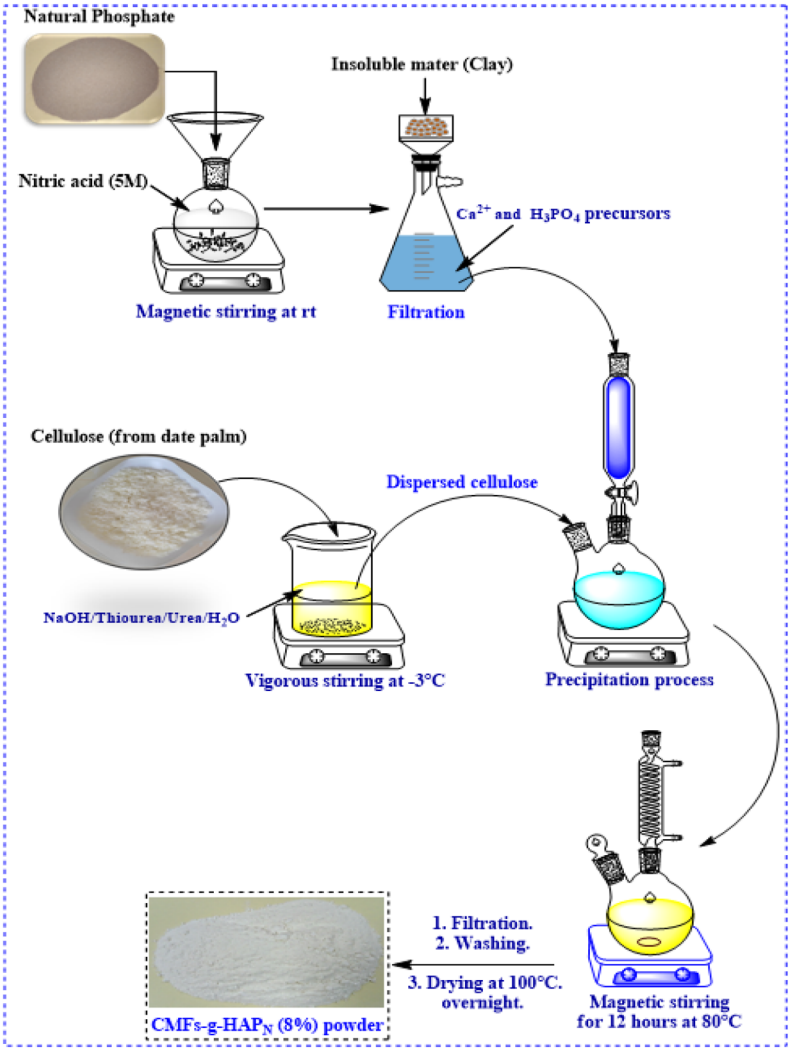


Cellulose was separated from the crushed raw DPF by an alkaline treatment process comprising three main steps. First, the DPF (5 wt %) was repeatedly washed with hot water (80 °C during 60 min) under vigorous mechanical agitation to extract the water-soluble components, mainly the hemicelluloses. The resulting residue was carefully hydrolyzed with alkaline NaOH solution (15 wt %) for 1 h at 80 °C under vigorous mechanical stirring to remove lignin. Then, the retained fibers obtained after the alkaline treatment were bleached with NaClO (1.7 wt % in water) and distilled water. The bleaching treatment was conducted at 85 °C for 1 h under mechanical stirring and was repeated twice. After each treatment, the fibers were filtered and washed with distilled water. Finally, after being ground and sieved ($\mu$m), the resulting bleached cellulose fibers, also known as cellulose microfibrils (CMFs), were oven-dried at 60 °C to remove excess of water. The process of CMF extraction is illustrated in Figure S4, Supporting Information.

**4.3. Preparation of CMFs-*g*-$HAP_N$ (8%).** The CMFs-*g*-$HAP_N$ (8%) preparation process was carried out in a 500 mL open glass reactor using Moroccan phosphate rock as calcium and phosphorus precursors and CMFs were extracted. First, about 100 g of NP was dissolved in 100 mL of $HNO_3$ (5 M) under continuous stirring at room temperature for 3 h. The insoluble matter was removed by centrifugation. Then, a certain amount of CMFs (corresponding to a grafting rate of 8%) was dispersed in 50 mL of a solution containing NaOH/thiourea/urea/$H_2O$ of 12:4.87:6:27.13 by weight under vigorous stirring at a cooling bath of −3 °C. The obtained mixture was then sonicated for a specific time using an ultrasonic system. 50 mL of the resulting CMF suspension was added gradually to 100 mL of the solution containing phosphorus and calcium precursor ions prepared previously from NP; NaOH (24%) was used to adjust the solution pH to 11. The resulting precipitate was magnetically stirred at 80 °C for 12 h. After that, a white precipitate of CMFs-*g*-$HAP_N$ (8%) is obtained by filtration, which is then washed several times with deionized water to get rid-off any unreacted space such as calcium and phosphate ions, before being dried at 100 °C overnight. We also prepared the natural hydroxyapatite as a reference material using the same preparation conditions without adding the cellulose polymer. The schematic illustration of the preparation process of CMFs-*g*-$HAP_N$ (8%) from NP and CMFs is shown in Scheme 2.

**4.4. CMFs-*g*-$HAP_N$ (8%) Characterization.** XRD patterns were obtained at room temperature on a Bruker AXS D-8 diffractometer using Cu-K$\alpha$ radiation in Bragg−Brentano geometry ($\theta$−2$\theta$). FTIR spectroscopy was performed with


https://doi.org/10.1021/acsomega.2c02108
ACS Omega 2022, 7, 28076−28092

an Affinity-1S SHIMADZU spectrometer equipped with a Golden Gate single reflection ATR accessory. TGA was conducted under air in a TA Instrument Q500 apparatus with a 10 °C/min ramp between 25 and 1000 °C. The surface morphology and local chemical composition of adsorbents were investigated using a field-emission scanning electron microscope (Tecnai G2 microscope at 120 kV) and energy-dispersive X-ray analysis, respectively. The specific surface area was determined from the nitrogen adsorption/desorption isotherms (at-196 °C) and measured with a Quanta-chrome Autosorb-1 automatic analyzer using the BET equation. The local chemical structure around phosphorus atoms was examined by solid-state $^{31}$P-nuclear magnetic resonance under magic angle spinning conditions (MAS-NMR) spectroscopy on a Bruker.

**4.5. Batch Adsorption Studies.** The adsorption experiments of Pb(II) and Cu(II) were conducted in Erlenmeyer flasks containing 50 mL of metal solutions with different concentrations of 60−100 mg/L and the appropriate amount of CMFs-*g*-HAP$_N$ (8%) as an adsorbent. The Erlenmeyer flasks were stirred under a constant speed of 200 rpm on a magnetic stirrer for different time intervals ranging from 30 to 90 min. The effects of three operating process parameters, namely, contact time, initial metal concentration, and adsorbent amount were studied simultaneously using BBD. After adsorption processes, the resulting mixtures were filtered and the residual concentration of Pb(II) and Cu(II) ions was measured using an atomic absorption spectrometer with suitable hollow cathode lamps at a wavelength of 283.3 and 324.8 nm, respectively. Thermodynamic studies were undertaken by varying the temperature from 25 to 65 °C. The removal efficiency (%) and adsorption capacity ($q_t$, mg/g) were derived through eqs 12 and 13, respectively.

$$\text{Removal}\ (\%) = \frac{C_0 - C_t}{C_0} \times 100 \tag{12}$$

$$q_t(\text{mg/g}) = \frac{(C_0 - C_t)V}{W} \tag{13}$$

where $C_0$ is the initial metal ion concentration (mg/L), $C_t$ is the metal ion concentration at time $t$ (mg/L), and $V$ is the volume of the solution (L) and $W$ is the weight of the adsorbent (g).

Preliminary series of Pb(II) and Cu(II) batch adsorption experiments were conducted to evaluate the stability of the HAP$_N$ and CMFs-*g*-HAP$_N$ and to ascertain at what level of CMF grafting (0, 4 and 8%) the highest removal efficiency could be attained. The results showed that the introduction of CMFs into the apatite matrix enhanced the removal efficiency of both studied metals and that the CMFs-*g*-HAP$_N$ (8%) adsorbent offered the highest removal efficiency; therefore, it would be adopted in this study for further optimizations.

**4.6. BBD and Data Analysis.** In this research paper, the BBD included RSM was adopted to optimize the adsorption process efficiencies of Pb(II) and Cu(II). This three-level factorial design required 15 batch adsorption experiments to optimize the three chosen parameters on the removal efficiency (%) and adsorption capacity (mg g$^{-1}$) variations using CMFs-*g*-HAP$_N$ (8%) as an adsorbent. These parameters were selected based on literature reports for heavy metal adsorption as well as on the results of preliminary studies performed in the laboratory. The other parameters, namely temperature and Pb(II) and Cu(II) solution pH were fixed at 25 °C, 6.3, and 5.4 respectively. Table 9 presents the experimental domain with different level values of each factor.

**Table 9. Experimental Range and Levels in the BBD for Pb(II) and Cu(II) Removal**

| factors | levels | | |
|---|---|---|---|
| | low (−1) | center (0) | high (+1) |
| $X_1$: contact time (min) | 30 | 60 | 90 |
| $X_2$: initial concentration (mg/L) | 60 | 80 | 100 |
| $X_3$: adsorbent dose (mg) | 40 | 70 | 100 |

The experimental design data were analyzed using Nemrodw software, and the responses (adsorption removal and capacity) were fitted to a polynomial quadratic model using the following equation:

$$Y = b_0 + \sum b_i X_i + \sum b_{ii} X_i^2 + \sum b_{ij} X_i X_j + \varepsilon \tag{14}$$

With $\hat{Y}$ being the predicted response and $b_0$, $b_i$, $b_{ii}$, and $b_{ij}$ being the regression coefficients for the intercept, linear, quadratic, and interactions between the input variables, respectively. $X_i$, $X_i^2$, and $X_j$ are the levels of the independent factors in coded units and $\varepsilon$ is the model error.

The ANOVA was executed to validate the statistical significance of the regression model and 2D-3D surface plots were generated to determine the optimum operating conditions for high removal of heavy metals.

**4.7. Desorption and Regeneration Study.** The recovery and reusability of a solid adsorbent are some of the most important features in practical applications for wastewater treatment. For this reason, desorption experiments were undertaken in order to assess the effects of different eluents on the desorption of Pb(II) and Cu(II) from CMFs-*g*-HAP$_N$ (8%). At first and right after equilibrium, the CMFs-*g*-HAP$_N$ (8%) loaded with Pb(II) or Cu(II) was centrifuged, then rinsed, and dried at 80 °C overnight. Subsequently, 40 mg of collected CMFs-*g*-HAP$_N$ (8%) was introduced to 50 mL of EDTA-Na$_2$ (0.01 M), oxalic acid (0.01 M), NaOH (0.1 M), and ethanol (0.1 M), respectively, while stirring at room temperature for 120 min. After the experiments, the concentration of Pb(II) or Cu(II) in each eluent was measured by AAS. Then, the best eluent was applied to reuse the CMFs-*g*-HAP$_N$ (8%) for three adsorption/desorption cycles. The mixture was stirred on a magnetic agitator for 120 min. The adsorbent was then filtered, washed thoroughly with distilled water, and finally stored in distilled water until use.

**4.8. Coexisting Cation Effect and Selectivity Testing.** Because wastewater generally contains a variety of ions, the efficiency of the prepared adsorbent is worth exploring in a multi-ion system, as this can help to assess the selectivity of the CMFs-*g*-HAP$_N$ (8%) and also study the effect of coexisting ions on its performance.[23,25] The effects of the most current ions in wastewater, namely, divalent ($Ca^{2+}$ and $Mg^{2+}$) and monovalent ($Na^+$) were studied by adding 0.01 M of NaCl, $CaCl_2$, $MgSO_4$, or a mixture of these (0.01 M for each) to a 50 mL solution of Pb(II), Cu(II) (single system), or both metals (binary system). Typically, 40 mg of CMFs-*g*-HAP$_N$ (8%) was mixed with 50 mL of solutions containing a mixture of Pb(II), Cu(II), and the aforementioned cations at room temperature during 60 min. The concentration of Pb(II) and Cu(II) was set at 100 ppm with different ratios (100:0 Pb:Cu or 0:100


https://doi.org/10.1021/acsomega.2c02108
ACS Omega 2022, 7, 28076−28092

Pb:Cu) regarding the single system and (50:50 Pb:Cu) in the binary system.

## ■ ASSOCIATED CONTENT

### Supporting Information

The Supporting Information is available free of charge at https://pubs.acs.org/doi/10.1021/acsomega.2c02108.

Design matrix for three coded variables together with the actual and predicted responses (Table S1), ANOVA for Pb(II) and Cu(II) removal efficiency (%) onto the CMFs-*g*-$HAP_N$ (8%) adsorbent (Table S2), estimates and statistics of the coefficients for Pb(II) and Cu(II) adsorption capacity (mg/g) and removal efficiency (%) (Table S3), graphical plot of predicted vs actual values of (a) Pb(II) adsorption capacity (mg/g), (b) Pb(II) removal efficiency (%), (c) Cu(II) adsorption capacity (mg/g) and (d) Cu(II) removal efficiency (%) (Figure S1), XRD patterns of CMFs-*g*-$HAP_N$ (8%) after Cu(II) adsorption (a) and after Pb(II) adsorption (b) (Figure S2), FTIR spectra of pure CMFs-*g*-$HAP_N$ (8%) (a), CMFs-*g*-$HAP_N$ (8%) after Pb(II) adsorption (b) and after Cu(II) adsorption (c) (Figure S3), the process of CMF extraction from date palm (Figure S4), 2D-3D surface graphs of the effect of (a) initial Pb(II) concentration and contact time, (b) adsorbent dose and initial Pb(II) concentration, and (c) adsorbent dose and contact time on Pb(II) adsorption capacity (mg $g^{-1}$) by CMFs-$HAP_N$ (8%) (Figure S5) and 2D-3D surface graphs of the effect of (a) initial Cu(II) concentration and contact time, (b) adsorbent dose and contact time, and (c) adsorbent dose and initial Cu(II) concentration on Cu(II) adsorption capacity (mg $g^{-1}$) by CMFs-$HAP_N$ (8%) (Figure S6) (PDF)

## ■ AUTHOR INFORMATION


### Corresponding Authors

**Karim Dänoun** − *VARENA Center, Rabat Design, MAScIR Foundation, Rabat 10100, Morocco;* orcid.org/0000-0002-0867-3627; Email: k.danoun@mascir.ma

**Mohamed Zahouily** − *Laboratory of Materials, Catalysis & Valorization of Natural Resources, URAC 24, Faculty of Sciences and Technology, Hassan II University of Casablanca, Mohammedia 20650, Morocco; VARENA Center, Rabat Design, MAScIR Foundation, Rabat 10100, Morocco;* orcid.org/0000-0002-1396-3485; Email: m.zahouily@mascir.ma

### Authors

**Salah Eddine Marrane** − *Laboratory of Materials, Catalysis & Valorization of Natural Resources, URAC 24, Faculty of Sciences and Technology, Hassan II University of Casablanca, Mohammedia 20650, Morocco;* orcid.org/0000-0002-0597-7844

**Dalia Allouss** − *Laboratory of Materials, Catalysis & Valorization of Natural Resources, URAC 24, Faculty of Sciences and Technology, Hassan II University of Casablanca, Mohammedia 20650, Morocco;* orcid.org/0000-0003-4474-8718

**Said Sair** − *VARENA Center, Rabat Design, MAScIR Foundation, Rabat 10100, Morocco;* orcid.org/0000-0001-9115-3421

**Badr-Eddine Channab** − *Laboratory of Materials, Catalysis & Valorization of Natural Resources, URAC 24, Faculty of Sciences and Technology, Hassan II University of Casablanca, Mohammedia 20650, Morocco;* orcid.org/0000-0002-4584-2776

**Abdallah Rhihil** − *Laboratory of Materials, Catalysis & Valorization of Natural Resources, URAC 24, Faculty of Sciences and Technology, Hassan II University of Casablanca, Mohammedia 20650, Morocco;* orcid.org/0000-0002-5802-1782

Complete contact information is available at: https://pubs.acs.org/10.1021/acsomega.2c02108


### Notes

The authors declare no competing financial interest.

## ■ ACKNOWLEDGMENTS

The majority of this work was supported by Moroccan foundation for advanced science innovation and research (MASCIR) and Laboratory of Materials, Catalysis and Valorization of Natural Resources (LMaCaVa).

## ■ REFERENCES


(1) Fu, F.; Wang, Q. Removal of Heavy Metal Ions from Wastewaters: A Review. *J. Environ. Manage.* **2011**, *92*, 407−418.

(2) Jamshaid, A.; Hamid, A.; Muhammad, N.; Naseer, A.; Ghauri, M.; Iqbal, J.; Rafiq, S.; Shah, N. S. Cellulose-Based Materials for the Removal of Heavy Metals from Wastewater - An Overview. *ChemBioEng Rev.* **2017**, *4*, 240−256.

(3) Jung, K.-W.; Lee, S. Y.; Choi, J.-W.; Lee, Y. J. A Facile One-Pot Hydrothermal Synthesis of Hydroxyapatite/Biochar Nanocomposites: Adsorption Behavior and Mechanisms for the Removal of Copper(II) from Aqueous Media. *Chem. Eng. J.* **2019**, *369*, 529−541.

(4) Teow, Y. H.; Kam, L. M.; Mohammad, A. W. Synthesis of Cellulose Hydrogel for Copper (II) Ions Adsorption. *J. Environ. Chem. Eng.* **2018**, *6*, 4588−4597.

(5) Lim, C. S.; Shaharuddin, M. S.; Sam, W. Y. Risk Assessment of Exposure to Lead in Tap Water among Residents of Seri Kembangan, Selangor State, Malaysia. *Glob. J. Health Sci.* **2012**, *5*, 1−12.

(6) Robson, M. Methodologies for Assessing Exposures to Metals: Human Host Factors. *Ecotoxicol. Environ. Saf.* **2003**, *56*, 104−109.

(7) Zeledón-Toruño, Z.; Lao-Luque, C.; Solé-Sardans, M. Nickel and Copper Removal from Aqueous Solution by an Immature Coal (Leonardite): Effect of PH, Contact Time and Water Hardness. *J. Chem. Technol. Biotechnol.* **2005**, *80*, 649−656.

(8) Selatnia, A.; Boukazoula, A.; Kechid, N.; Bakhti, M. Z.; Chergui, A.; Kerchich, Y. Biosorption of Lead (II) from Aqueous Solution by a Bacterial Dead Streptomyces Rimosus Biomass. *Biochem. Eng. J.* **2004**, *19*, 127−135.

(9) Salman, S. A.; Asmoay, A. A.; El-Gohary, A.; Sabet, H. Evaluation of Human Risks of Surface Water and Groundwater Contaminated with Cd and Pb in the Southern El-Minya Governorate, Egypt. *Drink. Water Eng. Sci.* **2019**, *12*, 23−30.

(10) Chen, J. P.; Wang, L.; Zou, S.-W. Determination of Lead Biosorption Properties by Experimental and Modeling Simulation Study. *Chem. Eng. J.* **2007**, *131*, 209−215.

(11) Barakat, M. A. New Trends in Removing Heavy Metals from Industrial Wastewater. *Arab. J. Chem.* **2011**, *4*, 361−377.

(12) Meenakshi, S.; Viswanathan, N. Identification of Selective Ion-Exchange Resin for Fluoride Sorption. *J. Colloid Interface Sci.* **2007**, *308*, 438−450.

(13) Lahnid, S.; Tahaikt, M.; Elaroui, K.; Idrissi, I.; Hafsi, M.; Laaziz, I.; Amor, Z.; Tiyal, F.; Elmidaoui, A. Economic Evaluation of Fluoride Removal by Electrodialysis. *Desalination* **2008**, *230*, 213−219.




https://doi.org/10.1021/acsomega.2c02108
*ACS Omega* 2022, 7, 28076−28092

(14) Ndiaye, P. I.; Moulin, P.; Dominguez, L.; Millet, J. C.; Charbit, F. Removal of Fluoride from Electronic Industrial Effluentby RO Membrane Separation. *Desalination* **2005**, *173*, 25−32.
(15) Li, Y.; Yang, L.; Xu, Z.; Sun, Q. Separation and Recovery of Heavy Metals from Waste Water Using Synergistic Solvent Extraction. *IOP Conf. Ser. Mater. Sci. Eng.* **2017**, *167*, No. 012005.
(16) Ahmed, S. A. Batch and Fixed-Bed Column Techniques for Removal of Cu(II) and Fe(III) Using Carbohydrate Natural Polymer Modified Complexing Agents. *Carbohydr. Polym.* **2011**, *83*, 1470−1478.
(17) Zhao, X.; Wang, J.; Wu, F.; Wang, T.; Cai, Y.; Shi, Y.; Jiang, G. Removal of Fluoride from Aqueous Media by Fe3O4@Al(OH)3 Magnetic Nanoparticles. *J. Hazard. Mater.* **2010**, *173*, 102−109.
(18) Gu, Z.; Fang, J.; Deng, B. Preparation and Evaluation of GAC-Based Iron-Containing Adsorbents for Arsenic Removal. *Environ. Sci. Technol.* **2005**, *39*, 3833−3843.
(19) Yunus Pamukoglu, M.; Kargi, F. Removal of Copper (II) Ions from Aqueous Medium by Biosorption onto Powdered Waste Sludge. *Process Biochem.* **2006**, *41*, 1047−1054.
(20) Ozdemir, G.; Ceyhan, N.; Ozturk, T.; Akirmak, F.; Cosar, T. Biosorption of Chromium (VI), Cadmium (II) and Copper (II) by Pantoea Sp. TEM18. *Chem. Eng. J.* **2004**, *102*, 249−253.
(21) Cooney, D. O. *Adsorption Design for Wastewater Treatment*; CRC press, 1998.
(22) Smičiklas, I.; Onjia, A.; Raičević, S.; Janaćković, Đ.; Mitrić, M. Factors Influencing the Removal of Divalent Cations by Hydroxyapatite. *J. Hazard. Mater.* **2008**, *152*, 876−884.
(23) Efome, J. E.; Rana, D.; Matsuura, T.; Lan, C. Q. Effects of Operating Parameters and Coexisting Ions on the Efficiency of Heavy Metal Ions Removal by Nano-Fibrous Metal-Organic Framework Membrane Filtration Process. *Sci. Total Environ.* **2019**, *674*, 355−362.
(24) Efome, J. E.; Rana, D.; Matsuura, T.; Lan, C. Q. Experiment and Modeling for Flux and Permeate Concentration of Heavy Metal Ion in Adsorptive Membrane Filtration Using a Metal-Organic Framework Incorporated Nanofibrous Membrane. *Chem. Eng. J.* **2018**, *352*, 737−744.
(25) Efome, J. E.; Rana, D.; Matsuura, T.; Lan, C. Q. Insight Studies on Metal-Organic Framework Nanofibrous Membrane Adsorption and Activation for Heavy Metal Ions Removal from Aqueous Solution. *ACS Appl. Mater. Interfaces* **2018**, *10*, 18619−18629.
(26) Efome, J. E.; Rana, D.; Matsuura, T.; Lan, C. Q. Metal−Organic Frameworks Supported on Nanofibers to Remove Heavy Metals. *J. Mater. Chem. A* **2018**, *6*, 4550−4555.
(27) Akram, M.; Ahmed, R.; Shakir, I.; Ibrahim, W. A. W.; Hussain, R. Extracting Hydroxyapatite and Its Precursors from Natural Resources. *J. Mater. Sci.* **2014**, *49*, 1461−1475.
(28) Yan, Y.; Dong, X.; Sun, X.; Sun, X.; Li, J.; Shen, J.; Han, W.; Liu, X.; Wang, L. Conversion of Waste FGD Gypsum into Hydroxyapatite for Removal of Pb2+ and Cd2+ from Wastewater. *J. Colloid Interface Sci.* **2014**, *429*, 68−76.
(29) Habibie, S.; Santosa Wargadipura, A. H.; Gustiono, D.; Herdianto, N.; Riswoko, A.; Nikmatin, S.; Clarke, S. Production and Characterization of Hydroxyapatite Bone Substitute Material Performed from Indonesian Limestone. *Int. J. Biomed. Eng. Sci.* **2017**, *4*, 11−23.
(30) Herliansyah, M. K.; Nasution, D. A.; Bin Abdul Shukor, M. H.; Ide-Ektessabi, A.; Wildan, M. W.; Tontowi, A. E. Preparation and Characterization of Natural Hydroxyapatite: A Comparative Study of Bovine Bone Hydroxyapatite and Hydroxyapatite from Calcite. *Mater. Sci. Forum* **2007**, *561-565*, 1441−1444.
(31) El Bamiki, R.; Raji, O.; Ouabid, M.; Elghali, A.; Khadiri Yazami, O.; Bodinier, J.-L. Phosphate Rocks: A Review of Sedimentary and Igneous Occurrences in Morocco. *Minerals* **2021**, *11*, 1137.
(32) Zahouily, M.; Elmakssoudi, A.; Mezdar, A.; Rayadh, A.; Sebti, S. Natural Phosphate and Potassium Fluoride Doped Natural Phosphate Catalysed Simple One-Pot Synthesis of α-Amino Phosphonates under Solvent-Free Conditions at Room Temperature. *Catal. Commun.* **2007**, *8*, 225−230.
(33) Dânoun, K.; Tabit, R.; Laghzizil, A.; Zahouily, M. A Novel Approach for the Synthesis of Nanostructured $Ag_3PO_4$ from Phosphate Rock: High Catalytic and Antibacterial Activities. *BMC Chem.* **2021**, *15*, 42.
(34) Shafiq, M.; Alazba, A. A.; Amin, M. T. Removal of Heavy Metals from Wastewater Using Date Palm as a Biosorbent: A Comparative Review. *Sains Malays.* **2018**, *47*, 35−49.
(35) Dalia, A.; Younes, E.; Chakir, A.; Samia, K.; Zahouily, M. Effective Removal of Cu(II) from Aqueous Solution over Graphene Oxide Encapsulated Carboxymethylcellulose-Alginate Hydrogel Microspheres: Towards Real Wastewater Treatment Plants. *Environ. Sci. Pollut. Res.* **2020**, *27*, 7476.
(36) Fernando, M. S.; de Silva, R. M.; de Silva, K. M. N. Synthesis, Characterization, and Application of Nano Hydroxyapatite and Nanocomposite of Hydroxyapatite with Granular Activated Carbon for the Removal of Pb2+ from Aqueous Solutions. *Appl. Surf. Sci.* **2015**, *351*, 95−103.
(37) Chen, S.; Zou, Y.; Yan, Z.; Shen, W.; Shi, S.; Zhang, X.; Wang, H. Carboxymethylated-Bacterial Cellulose for Copper and Lead Ion Removal. *J. Hazard. Mater.* **2009**, *161*, 1355−1359.
(38) Núñez, D.; Cáceres, R.; Ide, W.; Varaprasad, K.; Oyarzún, P. An Ecofriendly Nanocomposite of Bacterial Cellulose and Hydroxyapatite Efficiently Removes Lead from Water. *Int. J. Biol. Macromol.* **2020**, *165*, 2711−2720.
(39) Dalia, A.; Younes, E.; Amadine, O.; Chakir, A.; Zahouily, M. Response Surface Methodology for Optimization of Methylene Blue Adsorption onto Carboxymethyl Cellulose-Based Hydrogel Beads: Adsorption Kinetics, Isotherm, Thermodynamics and Reusability Studies. *RSC Adv.* **2019**, *9*, 37858−37869.
(40) Dânoun, K.; Jioui, I.; Bouhrara, M.; Zahouily, M.; Solhy, A.; Jouiad, M.; Len, C.; Fihri, A. Nano-Structured Pyrophosphate $Na_2CaP_2O_7$ as Catalyst for Selective Synthesis of 1, 2-Disubstituted Benzimidazoles in Pure Water. *Curr. Org. Chem.* **2015**, *19*, 2132−2140.
(41) Dânoun, K.; Essamlali, Y.; Amadine, O.; Tabit, R.; Fihri, A.; Len, C.; Zahouily, M. Nanostructured Pyrophosphate $Na_2PdP_2O_7$-Catalyzed Suzuki-Miyaura Cross-Coupling Under Microwave Irradiation. *Appl. Organomet. Chem.* **2018**, *32*, 4232.
(42) Jioui, I.; Dânoun, K.; Solhy, A.; Jouiad, M.; Zahouily, M.; Essaid, B.; Len, C.; Fihri, A. Modified Fluorapatite as Highly Efficient Catalyst for the Synthesis of Chalcones via Claisen−Schmidt Condensation Reaction. *J. Ind. Eng. Chem.* **2016**, *39*, 218−225.
(43) Dânoun, K.; Essamlali, Y.; Amadine, O.; Mahi, H.; Zahouily, M. Eco-Friendly Approach to Access of Quinoxaline Derivatives Using Nanostructured Pyrophosphate $Na_2PdP_2O_7$ as a New, Efficient and Reusable Heterogeneous Catalyst. *BMC Chem.* **2020**, *14*, 6.
(44) Tabit, R.; Amadine, O.; Essamlali, Y.; Dânoun, K.; Rhihil, A.; Zahouily, M. Magnetic $CoFe_2$ $O_4$ Nanoparticles Supported on Graphene Oxide (CoFe 2 O 4/GO) with High Catalytic Activity for Peroxymonosulfate Activation and Degradation of Rhodamine B. *RSC Adv.* **2018**, *8*, 1351−1360.
(45) Amedlous, A.; Amadine, O.; Essamlali, Y.; Dânoun, K.; Adil, M.; Zahouily, M. Aqueous-Phase Catalytic Hydroxylation of Phenol with $H_2O_2$ by Using a Copper Incorporated Apatite Nanocatalyst. *RSC Adv.* **2019**, *9*, 14132−14142.
(46) Rezki, B.; Younes, E.; Aadil, M.; Semlal, N.; Zahouily, M. Biodiesel Production from Rapeseed Oil and Low Free Fatty Acid Waste Cooking Oil Using a Cesium Modified Natural Phosphate Catalyst. *RSC Adv.* **2020**, *10*, 41065−41077.
(47) El Mansouri, A.; Oubella, A.; Dânoun, K.; Ahmad, M.; Neyts, J.; Jochmans, D.; Snoeck, R.; Andrei, G.; Morjani, H.; Zahouily, M. Discovery of Novel Furo[2,3-d] Pyrimidin-2-One−1,3,4-Oxadiazole Hybrid Derivatives as Dual Antiviral and Anticancer Agents That Induce Apoptosis. *Arch. Pharm. (Weinheim).* **2021**, *354*, No. e2100146.
(48) French, A. D.; Santiago Cintrón, M. Cellulose Polymorphy, Crystallite Size, and the Segal Crystallinity Index. *Cellulose* **2013**, *20*, 583−588.


https://doi.org/10.1021/acsomega.2c02108
*ACS Omega* 2022, 7, 28076−28092

(49) Narwade, V. N.; Khairnar, R. S.; Kokol, V. In Situ Synthesized Hydroxyapatite—Cellulose Nanofibrils as Biosorbents for Heavy Metal Ions Removal. *J. Polym. Environ.* **2018**, *26*, 2130−2141.
(50) Hokkanen, S.; Bhatnagar, A.; Repo, E.; Lou, S.; Sillanpä, M. Calcium Hydroxyapatite Microfibrillated Cellulose Composite as a Potential Adsorbent for the Removal of Cr (VI) from Aqueous Solution. *Chem. Eng. J.* **2016**, *283*, 445−452.
(51) Al-Saydeh, S. A.; El-Naas, M. H.; Zaidi, S. J. Copper Removal from Industrial Wastewater: A Comprehensive Review. *J. Ind. Eng. Chem.* **2017**, *56*, 35−44.
(52) Liu, Y.; Yan, Y.; Seshadri, B.; Qi, F.; Xu, Y.; Bolan, N.; Zheng, F.; Sun, X.; Han, W.; Wang, L. Immobilization of Lead and Copper in Aqueous Solution and Soil Using Hydroxyapatite Derived from Flue Gas Desulphurization Gypsum. *J. Geochem. Explor.* **2018**, *184*, 239−246.
(53) Liao, D.; Zheng, W.; Li, X.; Yang, Q.; Yue, X.; Guo, L.; Zeng, G. Removal of Lead(II) from Aqueous Solutions Using Carbonate Hydroxyapatite Extracted from Eggshell Waste. *J. Hazard. Mater.* **2010**, *177*, 126−130.
(54) Ko, D. C. K.; Cheung, C. W.; Choy, K. K. H.; Porter, J. F.; McKay, G. Sorption Equilibria of Metal Ions on Bone Char. *Chemosphere* **2004**, *54*, 273−281.
(55) Hillel, D. *Environmental Soil Physics*; Academic Press: San Diego. 1998.
(56) Orooji, Y.; Mortazavi-Derazkola, S.; Ghoreishi, S. M.; Amiri, M.; Salavati-Niasari, M. Mesopourous $Fe_3O_4$@$SiO_2$-Hydroxyapatite Nanocomposite: Green Sonochemical Synthesis Using Strawberry Fruit Extract as a Capping Agent, Characterization and Their Application in Sulfasalazine Delivery and Cytotoxicity. *J. Hazard. Mater.* **2020**, *400*, No. 123140.
(57) Hokkanen, S.; Repo, E.; Westholm, L. J.; Lou, S.; Sainio, T.; Sillanpä, M. Adsorption of Ni2+, $Cd^{2+}$, $PO_4^{3-}$ and $NO^{3-}$ from Aqueous Solutions by Nanostructured Microfibrillated Cellulose Modified with Carbonated Hydroxyapatite. *Chem. Eng. J.* **2014**, *252*, 64−74.
(58) Kushwaha, A.; Rani, R.; Patra, J. K. Adsorption Kinetics and Molecular Interactions of Lead [Pb(II)] with Natural Clay and Humic Acid. *Int. J. Environ. Sci. Technol.* **2020**, *17*, 1325−1336.
(59) Shalaby, T. I.; El-Kady, M. F.; Zaki, A. E. H. M.; El-Kholy, S. M. Preparation and Application of Magnetite Nanoparticles Immobilized on Cellulose Acetate Nanofibers for Lead Removal from Polluted Water. *Water Sci. Technol. Water Supply* **2017**, *17*, 176−187.
(60) Mohammad, A. M.; Salah Eldin, T. A.; Hassan, M. A.; El-Anadouli, B. E. Efficient Treatment of Lead-Containing Wastewater by Hydroxyapatite/Chitosan Nanostructures. *Arab. J. Chem.* **2017**, *10*, 683−690.
(61) Ho, S.-H.; Chen, Y.; Yang, Z.; Nagarajan, D.; Chang, J.-S.; Ren, N. High-Efficiency Removal of Lead from Wastewater by Biochar Derived from Anaerobic Digestion Sludge. *Bioresour. Technol.* **2017**, *246*, 142−149.
(62) Soltani, H.; Belmokhtar, A.; Zeggai, F. Z.; Benyoucef, A.; Bousalem, S.; Bachari, K. Copper (II) Removal from Aqueous Solutions by PANI-Clay Hybrid Material: Fabrication, Characterization, Adsorption and Kinetics Study. *J. Inorg. Organomet. Polym. Mater.* **2019**, *29*, 841−850.
(63) Huang, Y.; Wu, H.; Shao, T.; Zhao, X.; Peng, H.; Gong, Y.; Wan, H. Enhanced Copper Adsorption by DTPA-Chitosan/Alginate Composite Beads: Mechanism and Application in Simulated Electroplating Wastewater. *Chem. Eng. J.* **2018**, *339*, 322−333.
(64) Elhassani, C. E.; Essamlali, Y.; Aqlil, M.; Nzenguet, A. M.; Ganetri, I.; Zahouily, M. Urea-Impregnated HAP Encapsulated by Lignocellulosic Biomass-Extruded Composites: A Novel Slow-Release Fertilizer. *Environ. Technol. Innov.* **2019**, *15*, No. 100403.


https://doi.org/10.1021/acsomega.2c02108
*ACS Omega* 2022, 7, 28076−28092